

**UCSF**

**UC San Francisco Electronic Theses and Dissertations**

**Title**

In vitro reconstitution of T cell receptor-mediated segregation of the CD45 phosphatase

**Permalink**

<https://escholarship.org/uc/item/4270r9b6>

**Author**

Carbone, Catherine Bianca

**Publication Date**

2018

Peer reviewed|Thesis/dissertation

In vitro reconstitution of T cell receptor-mediated segregation of the  
CD45 phosphatase

by

Catherine B. Carbone

DISSERTATION

Submitted in partial satisfaction of the requirements for the degree of

DOCTOR OF PHILOSOPHY

in

Cell Biology

in the

GRADUATE DIVISION

of the

UNIVERSITY OF CALIFORNIA, SAN FRANCISCO

Approved: 

Copyright 2018

by

Catherine Bianca Carbone

*Dedicated to Kristin.*

# ACKNOWLEDGEMENTS

The greatest joy of my PhD has been working with and learning from our community of scientists. Thanks to Ron for showing me science is playful. Thanks to Enfu Hui, Xiaolei Su, and Marcus Taylor for their relentless support and enthusiasm. Thanks to Nadja Kern for bringing life back to this research when the project was in its dullest moments. Thanks to Nico Stuurman for his cheerful good morning every single day and his exceptional ability and willingness to teach. Thanks to Adam Williamson for his knack for unearthing the interesting kernel in a scientific question, even when I doubted there was one to be found, and thanks to Meghan Morrissey for keeping everyone's feet on the ground. Thanks to Courtney Schroeder for being my role model.

Thanks to the graduate students in the lab—Melissa Hendershott, Erik Jonsson, Courtney Schroeder, Walter Huynh, Stefan Niekamp, Xiaowei Yan, Nadja Kern, Taylor Skokan—for their friendship and for each of their unique perspectives. Thanks to the post docs in the lab—Rui Dong, Iris Grossman, Kara McKinley, Meghan Morrissey, Yuxiao Wang, Jongmin Sung, Adam Williamson, Garrett Greenan, Ankur Jain, Marcus Taylor, Xiaolei Su, Enfu Hui, Gira Bhabha, Damien Ekiert, Rick McKenny, Marvin Tenenbaum, Susan Ribeiro, Hui-Chun Cheng, Aathi

Karunakaran—for making science a little less scary. Being a part of the Vale Lab has made me a better scientist and a better person.

Thanks to the outstanding scientists I worked with outside of the lab, who taught me that science is most fun when it is bigger than one person—Ricardo Fernandes, Leah Sibener, Matthew Birnbaum, Chris Garcia, Matt Paszek, Matt Rubashkin, Fuiboon Kai, Valerie Weaver, Sam Lord, Delaine Larson, Kurt Thorn, Bill Shin, Clare Waterman, Sonny Vo, Tom Goddard, Elaine Meng, Doug Tischer, Justin McLaurin, Orion Weiner, Jean Chung, William Huang, Darren McAfee, Jay Groves, David Patterson, Sam Liang, Robert Weber, Zev Gartner, Minsuk Kwak, Young-Wook Jun, Ben Moree, Ariel Notcovich,. Thanks to the community at the Marine Biological Laboratory in Woods Hole and the Genentech Hall 3<sup>rd</sup> floor neighborhood for turning me into a cell biologist. Thanks to past lab members, especially John James and Sarah Goodwin, for welcoming me into their science family. Thanks again to Ron for building these communities and allowing me to be a part of them.

Thanks to Barbara Panning, Kimberley Mowry, Dennis Clegg, Stacey Richards, Katie Pointer, Pat Bixler, Janey Cohen, and Phil von Phul for getting me here.

Thanks to my friends for inspiring me to be better and supporting me when I failed.

Thanks to my Mom and Dad for their boundless love.

Thanks to Kristin for making me who I am.

## PUBLISHED WORK

Chapter 2 is adapted from:

Carbone CB, Vale RD, Stuurman N. An acquisition and analysis pipeline for scanning angle interference microscopy. *Nat Methods*. 2016 Oct 31;13(11):897-898. doi: 10.1038/nmeth.4030.

Chapter 3 is adapted from:

Carbone CB, Kern N, Fernandes RA, Hui E, Su X, Garcia KC, Vale RD. In vitro reconstitution of T cell receptor-mediated segregation of the CD45 phosphatase. *Proc Natl Acad Sci USA*. 2017 Oct 17. doi: 10.1073/pnas.1710358114

## ABSTRACT

# **Reconstitution of T cell receptor-mediated segregation of the CD45 phosphatase**

**Catherine Bianca Carbone**

One of the most important cellular decisions made by the immune system is whether or not a T cell will activate after contacting an antigen presenting cell (APC). This choice occurs and is regulated at the site of contact between a T cell and an APC. A hallmark of this “immunological synapse” is the partitioning of membrane proteins to create biochemically distinct domains that initiate signaling. Though the importance of protein segregation at the immunological synapse has been appreciated for decades, the mechanism by which proteins partition into different domains and how partitioning is modulated for regulation were not well understood. In this study, I aimed to understand how receptor and co-receptor organization on the T cell membrane controls signaling.



# TABLE OF CONTENTS

## **1 Chapter One – Cell biology of TCR signaling**

1.1 Introduction .....	2
1.2 References .....	6

## **2 Chapter Two – An acquisition and analysis pipeline for scanning angle interference**

### **microscopy**

2.1 Abstract .....	12
2.2 Introduction .....	12
2.3 Results and Discussion .....	14
2.4 Code Availability .....	16
2.5 Supporting Information .....	17
2.6 Author Contributions .....	32
2.7 Acknowledgements .....	32
2.8 References .....	32

## **3 Chapter Three – In vitro reconstitution of T cell receptor-mediated segregation of the CD45 phosphatase.**

3.1 Significance .....	35
3.2 Abstract .....	35

3.3	Introduction .....	36
3.4	Results .....	38
3.5	Discussion .....	48
3.6	Materials and Methods .....	51
3.7	Supporting Information .....	57
3.8	Author Contributions .....	62
3.9	Acknowledgements .....	62
3.10	References .....	62
<b>4</b>	<b>Chapter Four – Concluding thoughts</b>	
4.1	Conclusion .....	69
4.2	References .....	71

# LIST OF TABLES

<b>3 Chapter Three – In vitro reconstitution of T cell receptor-mediated segregation of the CD45 phosphatase.</b>	
3.1 Table S1. Protein extracellular domain size estimates . . . . .	57

# LIST OF FIGURES

<b>2 Chapter Two – An acquisition and analysis pipeline for scanning angle interference microscopy</b>	
2.1 Implementation of SAIM pipeline to measure sample topography. . . . .	13
2.2 Height error introduced by calibration error. . . . .	29
2.3 Calibration using supported lipid bilayers . . . . .	30
2.4 Imaging fluorescent nanobeads . . . . .	31
<b>3 Chapter Three – In vitro reconstitution of T cell receptor-mediated segregation of the CD45 phosphatase.</b>	
3.1 Receptor–ligand binding induces CD45 segregation at membrane interfaces . . . . .	39
3.2 Characterization of partitioned GUV–SLB membrane–membrane interfaces . . . . .	41
3.3 Membrane topology is influenced by local protein composition . . . . .	43
3.4 TCR–pMHC binding induces CD45 segregation at GUV–SLB interfaces . . . . .	45
3.5 The inhibitory coreceptor PD-1 excludes CD45 and colocalizes with TCR . . . . .	47
3.6 PD-L1 is not excluded from FKBP-bound membrane interfaces . . . . .	58
3.7 FKBP molecules in partitioned domains do not readily exchange . . . . .	59
3.8 TCR–pMHC and FRB–FKBP exclude CD45 $R_0$ and CD45 $R_{ABC}$ but not SNAP. . . . .	60
3.9 PD-1 is a target for CD45 dephosphorylation . . . . .	61

## CHAPTER 1

# **Cell Biology of TCR signaling**

## 1.1 Introduction

**TCR Signaling.** Activation of T cells in the mammalian adaptive immune system is a fascinating and elegant example of cell signaling. T cells must respond with extremely high specificity in order to reliably differentiate between pathogen- and host- derived peptides, which vary by only one or a few amino acids. Additionally, T cells must activate robustly in response to only a few pathogen-derived peptide ligands while ignoring a high background of peptides derived from the organism itself. Upon identifying its cognate ligand, a T cell will undergo dramatic cellular reorganization and rewiring of the transcriptional program, followed by secretion of cytokines and proliferation.

T cells accomplish this feat using a multi-protein complex called T cell receptor (TCR). The TCR is activated by phosphorylation of cytosolic activation motifs upon binding to peptide-major histocompatibility complex (pMHC) presented by an APC. The phosphorylation state of the TCR immunoreceptor tyrosine-based activation motifs (ITAMs), is controlled by a Src-family kinase, Lck, and a transmembrane phosphatase CD45.

**The kinetic segregation model.** One principle that has emerged from this signaling system is that clustering of membrane proteins with different functionalities can create distinct domains with specialized biochemical activities.<sup>1-4</sup> Stereotyped partitioning of proteins has been observed for all manner of T cell proteins, including receptors, co-receptors, adhesion proteins, phosphatases, and kinases.<sup>1,5-9</sup> One proposed mechanism for TCR activation is segregation away from the phosphatase CD45 in response to ligand binding, which increases the half-life of the

phosphorylated species.<sup>4,10-11</sup> This hypothesis, called the kinetic segregation model, predicts that TCR activation occurs as a consequence of the ensemble activity of signaling proteins organizing in response to TCR-pMHC binding rather than a TCR-intrinsic, structurally transmitted signal.

Since this idea was originally proposed 25 years ago, mounting experimental evidence has suggested kinetic segregation may be biologically important. Observational investigation has shown that localization of kinases and phosphatases is consistent with activation by re-localization of biochemical activities.<sup>12-13</sup> Using chimeric or truncated signaling proteins, it has also been demonstrated that the small inter-membrane dimension of the TCR-pMHC complex, around 13 nm, and the large size of the extracellular domains of the phosphatase, around 25-40 nm, are critical for proper partitioning.<sup>14-19</sup>

**Cell biological observations of partitioning.** Initial observations of T cell-APC conjugates using light microscopy demonstrated that CD45 is excluded from the contact site.<sup>13</sup> Later, higher resolution TIRF using supported lipid bilayers as a mimic for the APC identified TCR microclusters as the relevant signaling scaffold for T cell activation, and demonstrated that CD45 is also excluded at a smaller scale from these TCR enriched sub-regions.<sup>7</sup>

Using a cellular reconstitution system, James et al demonstrated that size-dependent partitioning of the inhibitory phosphatase CD45 away from the TCR is both necessary and sufficient for activation of a reconstituted T cell.<sup>20</sup> In this artificial “T cell” with the minimal TCR signaling machinery ectopically expressed in an HEK cell, exclusion of CD45 by an artificial receptor-

ligand interaction was sufficient for T cell activation, and mis-localization of CD45 to TCR clusters using a small extracellular domain ablated signaling.

Similarly, Cordoba et al demonstrated that the CD45 extracellular domain, like the TCR-pMHC extracellular domain, could be exchanged with a structurally unrelated domain without disrupting the signal activation.<sup>16</sup> However, if the large size of the phosphatase extracellular domain was not maintained, there was enhanced colocalization with the TCR and an inhibitory effect on signaling. Together the James and Cordoba studies demonstrate that the relative sizes of the receptor and phosphatase extracellular domain is a critical parameter for signal activation.

**Computational models of kinetic segregation.** Since the idea of spatial segregation of molecules at immune cell-cell contacts based on size was first proposed,<sup>4</sup> several groups have tested computationally if the known physical parameters of a membrane-membrane interface were sufficient to explain the observed patterns of immune synapse protein localization.

Initial computational modeling demonstrated that binding and membrane bending could provide the driving force for self-assembly of differently sized receptor-ligand pairs into partitioned domains.<sup>21</sup> This work was soon followed up by Burroughs et al to integrate the free energy associated with bond stretching and seeding of partitioning by pre-existing spatial heterogeneity.<sup>22</sup> Though the Burroughs et al study introduced the idea of a glycocalyx, the localization of unbound large molecules, like CD45, was not explicitly modeled. In 2003 and 2004, further work examined how variation of binding energies and densities of molecules might lead to partitioning or non-partitioning scenarios.<sup>23-24</sup> In 2006, modeling work from the laboratory of



Anton Van der Merwe directly addressed the idea that spatial segregation of CD45 from the TCR would create locally phosphatase-depleted zones that could cause TCR triggering.<sup>25</sup> In this study, and a subsequent review, the term “kinetic segregation” was coined, and the model took its current shape.<sup>26</sup>

**Physical models of kinetic segregation.** Concurrent with the computational modeling, several groups developed physical models of membrane interfaces to test how membrane bound molecules could organize at contact sites. These studies sought to uncouple active partitioning mechanisms that operate in response to TCR activation from self-organizing forces that could cause activation.<sup>27</sup> Successful efforts to reconstitute molecular segregation at membrane-membrane interfaces have been made with dimerizing GFP molecules<sup>28</sup> and hybridizing strands of DNA<sup>29</sup> at synthetic membrane contacts. These studies show that laterally mobile molecules at membrane-membrane interfaces organize by height and locally deform the membrane to accommodate different molecular sizes, however they do not directly address how the physiologically relevant phosphatase and lower affinity receptor-ligand pairs might organize at the T cell-APC interface.

**The CD45 phosphatase.** CD45 has been written about extensively, including a comprehensive review by Hermiston et al.<sup>30</sup> Briefly, CD45 is a highly abundant transmembrane protein tyrosine phosphatase expressed by all nucleated blood cells. Homologs have been identified in mammals, birds and fish. The intracellular domain is comprised of a catalytically active phosphatase domain, and a membrane distal catalytically inactive phosphatase domain, which shares sequence and structural homology with the active domain. The intracellular domain is 95%

homologous across mammalian species. CD45 has broad substrate specificity. In T cells its substrates include the CD3 $\zeta$  and CD3 $\epsilon$  chains, Src family kinases including Lck, the tyrosine kinase Zap70, and the inhibitory co-receptor PD-1.

Unlike the intracellular domain, the extracellular domain has only 35% sequence similarity across mammalian species though the overall organization is well conserved. A definitive ligand for CD45 has not been identified. The extracellular domain is heavily N-glycosylated and contains three fibronectin type III repeats, a cysteine-rich region and an additional O-glycosylated variably spliced region containing the “A”, “B”, and “C” exons. Expression of different isoforms in T cells depends on maturation, activation and differentiation state. Studies of isoform-specific signaling in CD45-deficient cell lines and in CD45 exon 6-deficient mice reconstituted with different isoforms of CD45 have yielded controversial results. The conflicting data in the literature may be a result of differences in the genetic background, different stimuli used, or a failure to recapitulate equivalent and physiological levels of each isoform.

**Reconstituting TCR-mediated segregation of CD45.** There were two broad goals guiding the work presented in this dissertation: the first was to develop imaging tools to measure the topography of membrane-membrane contact sites, and the second was to use these imaging tools with other methods to better understand how protein segregation might occur in immune synapses and how it might be tuned, e.g. by different CD45 isoforms.

## 1.2 References

1. Grakoui A, et al. (1999) The immunological synapse: a molecular machine

- controlling T cell activation. *Science* 285(5425):221–7.
2. Monks CRF, Kupfer H, Tamir I, Barlow A, Kupfer A (1997) Selective modulation of protein kinase C- $\theta$  during T-cell activation. *Nature* 385(6611):83–86.
  3. Monks CRF, Freiberg BA, Kupfer H, Sciaky N, Kupfer A (1998) Three-dimensional segregation of supramolecular activation clusters in T cells. *Nature* 395(6697):82–86.
  4. Springer TA (1990) Adhesion receptors of the immune system. *Nature* 346(6283):425–434.
  5. Kaizuka Y, Douglass AD, Varma R, Dustin ML, Vale RD (2007) Mechanisms for segregating T cell receptor and adhesion molecules during immunological synapse formation in Jurkat T cells. *Proc Natl Acad Sci* 104(51):20296–20301.
  6. Rossy J, Owen DM, Williamson DJ, Yang Z, Gaus K (2013) Conformational states of the kinase Lck regulate clustering in early T cell signaling. *Nat Immunol* 14(1):82–89.
  7. Varma R, Campi G, Yokosuka T, Saito T, Dustin ML (2006) T Cell Receptor-Proximal Signals Are Sustained in Peripheral Microclusters and Terminated in the Central Supramolecular Activation Cluster. *Immunity* 25(1):117–127.
  8. Yokosuka T, et al. (2012) Programmed cell death 1 forms negative costimulatory microclusters that directly inhibit T cell receptor signaling by recruiting phosphatase SHP2. *J Exp Med* 209(6):1201–1217.
  9. Yokosuka T, et al. (2010) Spatiotemporal Basis of CTLA-4 Costimulatory Molecule-Mediated Negative Regulation of T Cell Activation. *Immunity* 33(3):326–339.
  10. Davis SJ, van der Merwe PA (1996) The structure and ligand interactions of CD2:

- implications for T-cell function. *Immunol Today* 17(4):177–187.
11. Anton van der Merwe P, Davis SJ, Shaw AS, Dustin ML (2000) Cytoskeletal polarization and redistribution of cell-surface molecules during T cell antigen recognition. *Semin Immunol* 12(1):5–21.
  12. Bunnell SC, et al. (2002) T cell receptor ligation induces the formation of dynamically regulated signaling assemblies. *J Cell Biol* 158(7):1263–75.
  13. Leupin O, Zaru R, Laroche T, Müller S, Valitutti S (2000) Exclusion of CD45 from the T-cell receptor signaling area in antigen-stimulated T lymphocytes. *Curr Biol* 10(5):277–80.
  14. Choudhuri K, et al. (2009) Peptide-major histocompatibility complex dimensions control proximal kinase-phosphatase balance during T cell activation. *J Biol Chem* 284(38):26096–105.
  15. Choudhuri K, Wiseman D, Brown MH, Gould K, van der Merwe PA (2005) T-cell receptor triggering is critically dependent on the dimensions of its peptide-MHC ligand. *Nature* 436(7050):578–82.
  16. Cordoba S-P, et al. (2013) The large ectodomains of CD45 and CD148 regulate their segregation from and inhibition of ligated T-cell receptor. *Blood* 121(21):4295–302.
  17. Irlles C, et al. (2003) CD45 ectodomain controls interaction with GEMs and Lck activity for optimal TCR signaling. *Nat Immunol* 4(2):189–97.
  18. Lin J, Weiss A (2003) The tyrosine phosphatase CD148 is excluded from the immunologic synapse and down-regulates prolonged T cell signaling. *J Cell Biol* 162(4):673–82.
  19. McCall MN, Shotton DM, Barclay AN (1992) Expression of soluble isoforms of rat

- CD45. Analysis by electron microscopy and use in epitope mapping of anti-CD45R monoclonal antibodies. *Immunology* 76(2):310–7.
20. James JR, Vale RD (2012) Biophysical mechanism of T-cell receptor triggering in a reconstituted system. *Nature* 487:64–69.
  21. Qi SY, Groves JT, Chakraborty AK (2001) Synaptic pattern formation during cellular recognition. *Proc Natl Acad Sci* 98(12):6548–6553.
  22. Burroughs NJ, Wülfing C (2002) Differential Segregation in a Cell-Cell Contact Interface: The Dynamics of the Immunological Synapse. *Biophys J* 83(4):1784–1796.
  23. Weikl TR, Lipowsky R (2004) Pattern Formation during T-Cell Adhesion. *Biophys J* 87(6):3665–3678.
  24. Lee S-JE, Hori Y, Chakraborty AK (2003) Low T cell receptor expression and thermal fluctuations contribute to formation of dynamic multifocal synapses in thymocytes. *Proc Natl Acad Sci* 100(8):4383–4388.
  25. Choudhuri K, Wiseman D, Brown MH, Gould K, van der Merwe PA (2005) T-cell receptor triggering is critically dependent on the dimensions of its peptide-MHC ligand. *Nature* 436(7050):578–582.
  26. Davis SJ, van der Merwe PA (2006) The kinetic-segregation model: TCR triggering and beyond. *Nat Immunol* 7(8):803–809.
  27. Rozdzial MM, Malissen B, Finkel TH (1995) Tyrosine-phosphorylated T cell receptor zeta chain associates with the actin cytoskeleton upon activation of mature T lymphocytes. *Immunity* 3(5):623–33.
  28. Schmid EM, et al. (2016) Size-dependent protein segregation at membrane interfaces. *Nat Phys* 12(7):704–711.

29. Chung M, Koo BJ, Boxer SG (2013) Formation and analysis of topographical domains between lipid membranes tethered by DNA hybrids of different lengths. *Faraday Discuss* 161:333–345.
30. Hermiston ML, Xu Z, Weiss A (2003) CD45: A Critical Regulator of Signaling Thresholds in Immune Cells. *Annu Rev Immunol* 21(1):107–137.

## CHAPTER 2

# **An acquisition and analysis pipeline for scanning angle interference microscopy**

Catherine B Carbone<sup>1,2</sup>, Ronald D Vale<sup>1,2</sup>, and Nico Stuurman<sup>1,2</sup>

<sup>1</sup>Department of Cellular and Molecular Pharmacology, University of California San Francisco, San Francisco, California, 94158. <sup>2</sup>Howard Hughes Medical Institute, San Francisco, California, 94158.

## 2.1 Abstract

We describe open-source software and hardware tools for calibrating, acquiring, and analyzing images for scanning angle interference microscopy (SAIM) analysis. These tools make it possible for a user with a total internal reflection fluorescence (TIRF) microscope equipped with a motorized illumination unit to generate reconstructed images with nanometer precision in the axial (z) direction and diffraction-limited resolution in the lateral (x, y) plane.

## 2.2 Introduction

Surface-generated fluorescence interference contrast methods, including SAIM, can help researchers determine the axial position or topography of biological structures by reporting the average vertical position within a diffraction-limited spot<sup>1,2,3</sup>. These methods have a powerful ability to examine largely unexplored dynamics of thin structures like membranes, adhesion complexes, and the cytoskeleton with nanometer accuracy in the axial direction<sup>3</sup>. Though SAIM utilizes relatively simple optics that are available on commercial microscopes, difficulties with calibration and the lack of available analysis software have hampered its widespread adoption. Here, we describe a tool for automated angle calibration and a freely available, open-source software, which together create a straightforward pipeline for SAIM analysis.

For interference contrast microscopy, the sample is placed on a transparent spacer on top of a mirror (silicon wafer with silicon oxide spacer; Fig. 1a and Supplementary Methods). Incident excitation light interferes with its own reflection (Fig. 1b), resulting in an intensity field that varies with axial distance in a theoretically predictable manner (Supplementary Note 1). Upon varying the angle of excitation, different intensity profiles can be obtained. By acquiring images



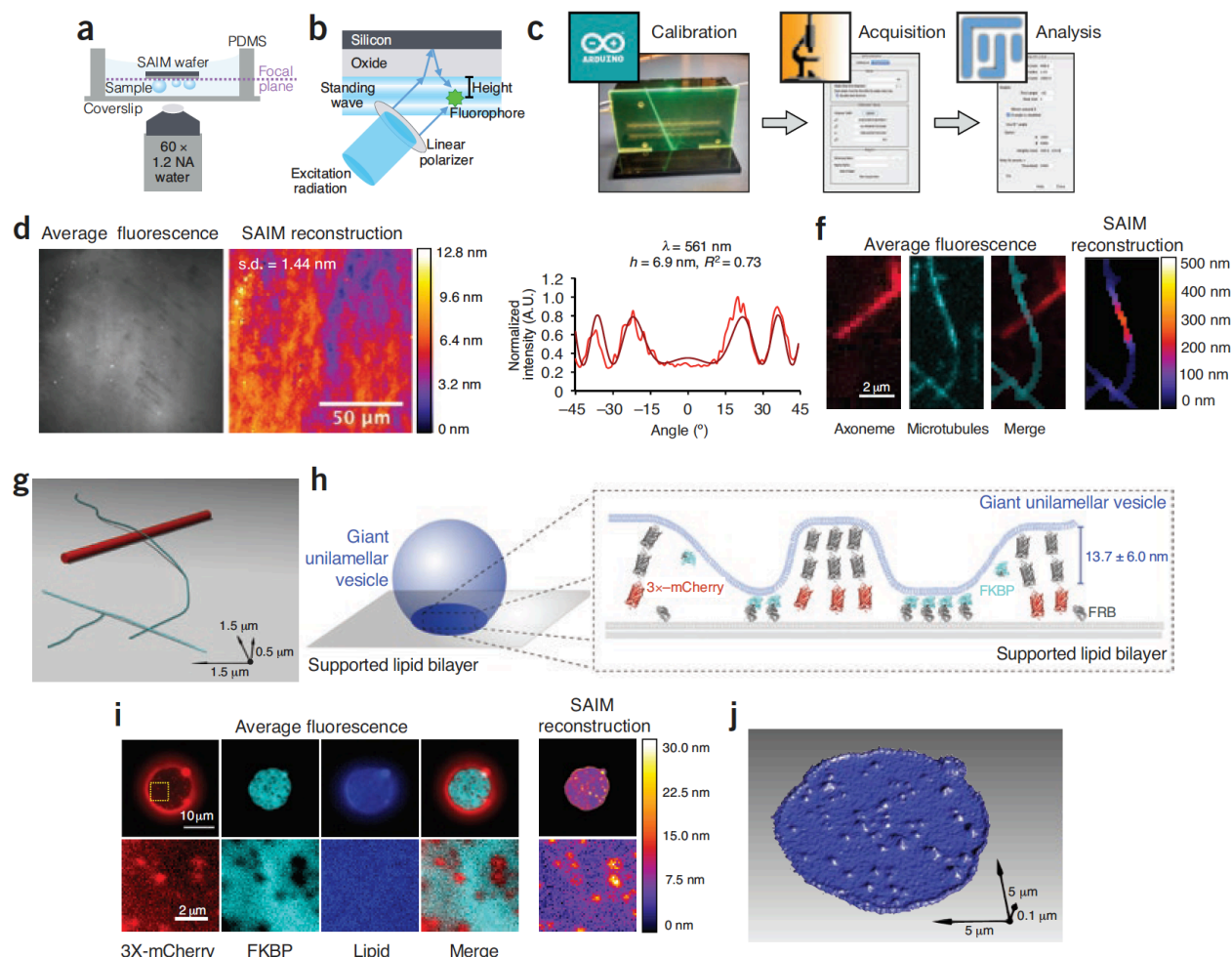


**Figure 1.** Implementation of SAIM pipeline to measure sample topography. **(a)** Schematic representation of sample setup for SAIM. A sample is assembled on a silicon oxide wafer, and then the wafer is inverted, submerged in buffer for imaging. **(b)** Schematic of SAIM theory. Patterned illumination is achieved by interference between incident and reflected excitation light. This pattern is dependent on the angle of illumination. **(c)** Schematic of SAIM tools. A  $\mu$ Manager controlled Arduino device is used to calibrate the angle of laser illumination, and then a  $\mu$ Manager plugin is used to acquire SAIM image sets. Finally these image sets are analyzed by a Fiji plugin to output a topographical map of the sample. **(d)** SAIM height of a supported lipid bilayer labeled with DiI. Left, mean fluorescence intensity across all angles sampled. Right, SAIM reconstruction showing a height standard deviation of 1.44 nm across a  $10,000 \mu\text{m}^2$  field. **(e)** Representative single pixel fit for supported lipid bilayer measurements. Raw data shown in light red, fit shown in dark red. **(f)** SAIM height of a microtubule crossing an axoneme. Left, mean fluorescence intensity for a Cy5 labeled axoneme (red) and Alexa 647 labeled microtubule (cyan). Right, SAIM reconstruction of microtubule height showing a representative deflection at the intersection with the axoneme and intersection with other microtubules. **(g)** 3D model of data shown in **c**. Microtubules are shown as cylinders with a radius of 12.5 nm along spline fits through SAIM data (cyan). The axoneme is modeled as a straight cylinder with a radius of 100 nm (red). **(h)** Schematic of membrane interface showing relative sizes of proteins used to form partitioned membrane regions based on published structures PDB: 2h5q and 3fap. **(i)** SAIM height of a membrane interface between a giant unilamellar vesicle (GUV) and a supported lipid bilayer (SLB). Left, mean fluorescence intensity for a GUV-tethered triple length mCherry (red), GUV-tethered Alexa647 labeled FKBP binding SLB-tethered FRB (cyan), Atto390 labeled GUV membrane (blue) and the merged mCherry and FKBP fluorescence images. Right, SAIM reconstruction of GUV membrane derived from Atto390 labeled lipid fluorescence showing representative deflection at mCherry clusters. **(j)** 3D model of data shown in **i**. Z-scale is exaggerated to clearly depict membrane deformations.

at multiple angles and fitting the intensities pixel by pixel to the theoretical prediction, one can determine the average height of each spatial element with nanometer accuracy.

## 2.3 Results and Discussion

Our SAIM pipeline begins with an automated calibration procedure (Fig. 1c, left; and Supplementary Note 2). We designed a simple apparatus, which is controlled with a plugin for the open-source mManager software<sup>4</sup> that defines the relation between motor position and angle of illumination. This device sits above the objective at the position of the sample. It consists of a transparent acrylic front plate that fluoresces upon illumination by a laser beam and two vertically spaced linear charge-coupled devices (CCDs) that localize the beam as it passes through the front plate (Supplementary Protocol). Compared with manual procedures, automated angle measurement provides a faster, more precise calibration. Automated calibration is especially advantageous for multicolor measurements, as it reduces the time required to calibrate each laser by about ten-fold. Furthermore, automated calibration is highly reproducible, minimizing errors in calibration, which can readily translate into height measurement errors of greater than 10 nm (Supplementary Fig. 1).

After calibration, the sample is imaged at varying angles of illumination by controlling a motorized illuminator with the mManager plugin (Fig. 1c, middle)<sup>4</sup>. Next, these images are analyzed to generate a topographical map (Fig. 1c, right). Our analysis software is a Fiji<sup>5</sup> plugin that (i) plots the predicted excitation intensity at a given distance from the surface of the oxide layer as a function of angle, (ii) fits the theoretical model to an experimentally determined intensity profile at a given region of interest (ROI), and (iii) carries out fits for all pixels in an

image (Supplementary Note 3). The calibration and acquisition plugin is independent from the analysis plugin; however, they can be used within the same package because they both run in ImageJ.

Samples for SAIM are prepared on silicon substrates with an oxide spacer. To measure absolute height of a sample, it is critical to know the precise thickness of the oxide spacer. We measured the oxide thickness of SAIM substrates using ellipsometry (Supplementary Fig. 2b). We also estimated oxide spacer thickness using SAIM (Supplementary Fig. 2b,c). We recommend performing this measurement on the day of an experiment to minimize variability that is caused by changes in the microscope and/or calibrations (Supplementary Fig. 2d and Supplementary Note 4). Once calibrated, this technique can be used to measure the height of a lipid bilayer with a standard deviation around 1 nm at approximately 106 photons per pixel (Fig. 1d,e and Supplementary Fig. 2e).

To test accuracy and limitations of SAIM and our analysis pipeline, we measured nanometer-scale height changes in samples of biomolecules with known sizes (also see Supplementary Note 5 and Supplementary Fig. 3). First, we measured the deformation of a microtubule (25-nm diameter) as it crossed on top of an axoneme (a rigid structure of microtubules with a diameter of about 200 nm). The average microtubule height change at an axoneme crossing was measured by our SAIM technique to be  $227 \pm 44$  nm ( $n = 6$ , one replicate; Fig. 1f, modeled in Fig. 1g). Next, we measured the deformation of a lipid membrane at a membrane interface consisting of a giant unilamellar vesicle interacting with a supported lipid bilayer and separated by protein spacers of two different heights (5 nm for FRB–rapamycin–FKBP and 18 nm for a 3X–mCherry; Fig. 1h).

The height difference caused these proteins to segregate from one another into distinct domains (Fig. 1i) (ref. 6). The membrane height change at a 3X-mCherry cluster relative to an adjacent FRB-rapamycin-FKBP domain was  $13.7 \pm 6.0$  nm ( $n = 157$  clusters from five giant unilamellar vesicle (GUVs) imaged during two separate experiments; Fig. 1i,j), as measured by our SAIM pipeline. This result is consistent with the expected height difference (Fig. 1h) and similar to values obtained by reflection interference contrast microscopy for an analogous membrane deformation experiment<sup>6</sup>.

These open-source tools should greatly facilitate the implementation of SAIM for studying the axial organization of fluorescently tagged molecules at nanometer scales.

## 2.4 Code Availability

SAIM analysis and mManager acquisition software (Supplementary Software) are available under the Berkeley Software Distribution (BSD) license.

Full documentation and examples are available at the project pages:

<http://imagej.net/Saim>

<https://valelab.ucsf.edu/~kcarbone/SAIM>

Development is hosted on GitHub at:

<https://github.com/valelab/saimAnalysis>

<https://github.com/valelab/saimCalibration>.

## 2.5 Supporting Information

**Supplementary Note 1.** Formulas for SAIM analysis. Formulas used for the analysis plugin are drawn from supplementary reference [1]. This reference contained a typographical error in the  $r^{TE}$  formula (3), which has been corrected here.

For incident light polarized perpendicular to the plane of incidence, the detected intensity variation at a given pixel in the image relates to the average height of the fluorophore and the angle of incidence as follows:

$$I = A(|1 + r^{TE} e^{i\phi(H)}|)^2 + B \quad (1)$$

where:

A – accounts for variation in detected intensity due to factors including mean excitation laser intensity, fluorophore density, efficiency of emitted photon detection, etc..

B – is an offset parameter that accounts for background fluorescence in the sample images.

H – is the position above the silicon oxide layer

$\phi(H)$  – the phase difference of the direct and reflected light at axial position H given by:

$$\phi(H) = \frac{4\pi}{\lambda} (n_b H \cos\theta_b) \quad (2)$$

$r^{TE}$  – the effective Fresnel coefficient obtained from the transfer matrix  $m^{TE}$  according to:

$$r^{TE} = \frac{(m_{11}^{TE} + m_{12}^{TE} p_0) p_2 + (m_{21}^{TE} - m_{22}^{TE} p_0)}{(m_{11}^{TE} + m_{12}^{TE} p_0) p_2 + (m_{21}^{TE} + m_{22}^{TE} p_0)} \quad (3)$$

where:

$$m_{11}^{TE} = \cos(k_{0x} d_{ox} \cos\theta_{ox}) \quad (4)$$

$$m_{12}^{TE} = \frac{-i}{p_1} \sin(k_{0x} d_{ox} \cos\theta_{ox}) \quad (5)$$

$$m_{21}^{TE} = -ip_1 \sin(k_{0x} d_{ox} \cos\theta_{ox}) \quad (6)$$

$$m_{22}^{TE} = \cos(k_{0x} d_{ox} \cos\theta_{ox}) \quad (7)$$

$$p_0 = n_{Si} \cos\theta_{Si}, p_1 = n_{ox} \cos\theta_{ox}, p_2 = n_b \cos\theta_b \quad (8)$$

$$k_i = \frac{2\pi n_i}{\lambda} \quad (9)$$

$k_i$  – wavenumber in the given material

$n_{Si}$  – refractive index of silicon

$n_{ox}$  – refractive index of the oxide layer

$n_b$  – refractive index of the sample

$\theta_{Si}$  – angle of incidence in the silicon

$\theta_{ox}$  – angle of incidence in the oxide layer

$\theta_b$  – angle of incidence in the sample

By rewriting the effective Fresnel coefficient as a complex number:

$$r^{TE} = c + id \quad (10)$$

Equation 1 can then be rewritten as:

$$I = A(1 + 2ccos\phi(H) - 2dsin\phi(H) + c^2 + d^2) + B \quad (11)$$

Not only can equation 11 be computed about 10 times faster than equation 1, it can also be used to derive partial derivatives needed for Levenberg-Marquard non-linear least square curve fitting, using

$$f = \frac{d}{dH} \phi(H) = \frac{4\pi n_b \cos\theta_b}{\lambda} \quad (12)$$

Partial derivative of equation 11 for H:

$$\frac{d}{dH} (I) = -2Af(csin\phi(H) + dcos\phi(H)) \quad (13)$$

**Supplementary Note 2.** Additional information about calibration. The SAIM calibration device is based on an Arduino open-source electronics platform. The device uses two linear CCDs (AMS-TAOS USA Inc., TSL-1412S) positioned above the microscope objective lens to detect

fluorescence emitted by an acrylic faceplate when illuminated by an excitation laser (**Fig. 1d**, left). Based on the known, fixed vertical displacement between these two detectors the angle of that excitation light can be determined (**Supplementary Protocol**). The device is sized to fit in a standard 96-well plate stage insert.

The calibration device is controlled by a  $\mu$ Manager [5] plugin to execute SAIM calibration and data acquisition. This plugin consists of two parts. 1) The “Calibration” panel communicates with the calibration device and defines the relation between the refractive index corrected angle of excitation light and position of a motorized TIRF illuminator by fitting the data with a cubic polynomial and storing the function parameters. The plugin will store calibrations for multiple channel groups that can be accessed from the acquisition panel. 2) The “Acquisition” panel reads the calibration for a given channel group, takes a user provided range of angles and the number of steps for sampling this range, and then runs a series of acquisitions at these angles.

**Supplementary Note 3.** Additional information about analysis plugin. This SAIM analysis software is a FIJI [6] plugin consisting of three parts. "SAIM Plot" plots theoretical predictions for the intensity distribution as a function of distance from the surface of the oxide layer. "SAIM Inspect" and "SAIM Fit" are very similar; however, SAIM Inspect will act on the average values of the ROI (for instance, the pixel under the cursor) and executes only a single fit, whereas SAIM Fit will analyze all pixels of the image stack. SAIM Fit will fit each pixel in the input stack and output a stack with 4 images. The first one is the height map (in nm), the second image has the r-squared values (an indication of the goodness of fit with values between 0 and 1, the closer to 1, the better the fit), the third image shows the values for "A", a scaling parameter that

accounts for variation in intensity, and the last image shows the values for "B", an offset parameter that accounts for background fluorescence. For samples thicker than one half the wavelength of excitation light, both the Fit and Inspect tools can be given multiple starting heights to prevent the fitting code from getting stuck in local minima.

This plugin uses the equations from the Paszek et al. paper [Supplementary reference 1] with a few extensions (**Supplementary Note 1**). The code uses an unbounded Levenberg-Marquard optimizer that minimizes the square of the difference between observed and predicted values. Parameters are restricted to physically relevant values (for instance, no negative heights are allowed). Execution speed depends on image content, though we routinely analyze every pixel in a dataset of 86 images at 1024 x 1024 pixels in 2.5 minutes on a MacBook Pro with a 2.7 GHz Intel Core i5 processor. In practice, masking images to fit only relevant pixels can accelerate processing dramatically.

**Supplementary Note 4.** Measurement of exact oxide thickness. Samples for SAIM are prepared on commercially available silicon substrates with an oxide spacer. Any thickness of the oxide spacer can be used, but we found that spacers of ~1900 nm provided the optimal periodicity of the SAIM function in the range of angles that could be sampled using a 1.20 NA water immersion objective (**Supplementary Fig. 2a**). We measured the oxide thickness of SAIM substrates using ellipsometry (**Supplementary Fig. 2b**). To perform SAIM measurements without access to an ellipsometer, oxide spacer thickness also can be estimated using SAIM. We imaged a monolayer of surface-bound fluorescent dyes of defined thickness and fit theoretical predictions for different oxide heights to the data until the known height of the sample was



derived. This method will also correct for differences in apparent oxide height for multiple laser lines. We used a DiO, DiI, and DiD triple labeled supported lipid bilayer (SLB) for this purpose, and fit the oxide to the known height of 6.4 nm for a phospholipid bilayer (**Supplementary Fig. 2b-c**)[Supplementary reference 10]. In our experiments the apparent oxide height varied by as much as 10-20 nm between experiments; therefore, we recommend performing this measurement on the day of each experiment to minimize variability in measurements due to changes in the microscope and/or calibrations (**Supplementary Fig. 2d**).

**Supplementary Note 5.** Comments on imaging complex samples. The SAIM theory predicts intensity as a function of angle of the excitation light for a point source with infinitesimal axial dimensions. In practice, fluorophores may be distributed over multiple z-positions within a diffraction-limited spot [Supplementary references 2-8], and the measured fluorescence signal is the sum of the individual contributions of each fluorophore. The resulting intensity versus excitation angle curve is not necessarily representative of the averaged z-heights.

Small (40-200nm) fluorescent nano-sized beads have regularly been used to validate SAIM measurements, using the assumption that the height in SAIM is the bead radius [3]. To address this assumption, we modeled the appearance of a 200nm sphere, stained throughout, in SAIM. The model divides the sphere in 9 parts, calculates the SAIM curve for each part, and averages the predicted intensity for the 9 parts at each angle, weighted by the fraction of the sphere's volume contained in each part (**Supplementary Fig. 3a**). This model shows that the bead's SAIM curve resembles the SAIM curve of a point source at the radius of the bead; however, the intensity maxima and minima are lower, especially at low angles. Fitting the resulting data with

the SAIM Inspect tool resulted in a predicted height of 99.4 nm ( $r^2$  of 0.93), similar to the radius of the bead.

We measured fluorescent beads using both SAIM and negative stain electron microscopy. For SAIM, beads were adsorbed onto silicon substrates with an oxide spacer of  $\sim 1900$  nm. Angle dependent changes in bead fluorescence intensity were fit to the optical model to obtain the axial position of the bead center. These measurements were repeated for beads with nominal 20- or 50-nm radii, and fluorescence excitation wavelengths of 488 or 561 nm (**Supplementary Fig. 3b**). Though the optical model predicts that fluorescent nanobeads should be reliably fit by the SAIM function, we found that SAIM heights were consistently around 10 nm larger than heights derived from EM measurement (**Supplementary Fig. 3c**). This offset is consistent with previously published results using SAIM to measure fluorescent bead heights [3]. For this reason, we advise using fluorescent monolayers instead of fluorescent beads for SAIM validation going forward.

For fluorescent beads the distribution of fluorophores is well defined and easily modeled. However, the distribution of fluorophores in a biological sample, like a fixed cell stained with fluorescent antibody is more difficult to predict. In cases of thicker samples, careful sample preparation to minimize background is key. SAIM is theoretically capable of measuring heights up to 1  $\mu\text{m}$  or so using multiple starting z-heights for the fitting code, but obtaining reliable data with enough photons and minimal photobleaching can be challenging.

**Supplementary Methods.**

**Optical setup.** SAIM imaging was performed on one of two Nikon TI-E microscopes equipped with a Nikon 60x Plan Apo VC 1.20 NA water immersion objective, and four laser lines (405, 488, 561, 640 nm), either a Hamamatsu Flash 4.0 or Andor iXon EM-CCD camera, and  $\mu$ Manager software [5]. A polarizing filter was placed in the excitation laser path to polarize the light perpendicular to the plane of incidence. Angle of illumination was controlled with either a standard Nikon TIRF motorized positioner or a mirror moved by a motorized actuator (Newport, CMA-25CCCL).

**Preparation of reflective substrates with adsorbed nanobeads.** N-type silicon wafers with  $1900 \text{ nm} \pm 5\%$  thermal oxide were purchased from Addison Engineering. Wafers were cut to approximately  $1 \text{ cm}^2$  using a diamond tipped pen and cleaned using air plasma for five min at a radio frequency of 18W (Harrick Plasma). 40- or 100-nm carboxylate-modified yellow-green, orange, or red fluorescent spheres (Invitrogen) were diluted in 70% ethanol, added to the wafers, and dried in a vacuum desiccator. The wafers were then washed vigorously with water, air-dried, and stored at room temperature.

**Electron microscopy.** 40- or 100-nm carboxylate-modified yellow-green, orange, or red fluorescent spheres (Invitrogen) were prepared by 100- to 500-fold dilution into 70% ethanol followed by sonication. To prepare grids for negative stain EM, samples were applied to freshly glow discharged carbon coated 400 mesh copper grids and blotted off. Immediately after blotting, a 2% uranyl formate solution was applied for staining and blotted off. The stain was applied five times per sample. Samples were allowed to air dry before imaging. Data were collected on a Tecnai T12 microscope (FEI) equipped with a 4K x 4K CCD camera (UltraScan

4000, Gatan). 100 nm nanobeads were imaged with a pixel size of 0.58 pixels per 1 nm and magnification of 6,500x, and 40 nm nanobeads were imaged with a pixel size of 0.98 pixels per 1 nm magnification of 11,000x.

**Preparation of reflective substrates with supported lipid bilayers.** Silicon wafers with 1900 nm oxide spacers were obtained from Addison Engineering, cut, and cleaned using the same process as for for nanobead imaging. Synthetic 1,2-dioleoyl-*sn*-glycero-3-phosphocholine (POPC; Avanti, 850457), 1,2-dioleoyl-*sn*-glycero-3-[(N-(5-amino-1-carboxypentyl)iminodiacetic acid)succinyl] (nickel salt, DGS-NTA-Ni; Avanti, 790404) and 1,2-dioleoyl-*sn*-glycero-3-phosphoethanolamine-N-[methoxy(polyethylene glycol)-5000] (ammonium salt, PEG5000-PE; Avanti, 880220) were purchased from Avanti Polar Lipids. Small unilamellar vesicles (SUVs) were prepared from a mixture of 95.5% POPC, 2% DGS-NTA-Ni, and 0.5% PEG5000-PE. The lipid mixture in chloroform was evaporated under argon and further dried under vacuum. The mixture was then rehydrated with phosphate buffered saline pH 7.4 and cycled between -80°C and 37°C 20 times, and then centrifuged for 45 min at 35,000 RCF. SUVs made by this method were stored at 4°C and used within two weeks of formation. To make labeled supported lipid bilayers, wafers were submerged in PBS in freshly plasma cleaned custom PDMS chambers on RCA cleaned glass coverslips. 100 µl of SUV solution containing 0.5 to 1 mg/ml lipid was added to the coverslips and incubated for 30 min. Unadsorbed vesicles were removed by washing three times with PBS, then bilayers were stained for 20 min with approximately 100 ng/mL DiO, DiI and/or DiD solution in PBS (Invitrogen). Wafers were again washed three times with PBS. The wafer is subsequently inverted in the imaging chamber prior to imaging.

**Preparation of microtubules.** Tubulin was purified from pig brain, and biotinylated or fluorescently labeled tubulin were prepared as described [Supplementary reference 11]. A mixture of unlabeled tubulin, biotin-tubulin, and fluorescent tubulin (~10:1:1 ratio) was assembled in BRB80 (80 mM PIPES, 1 mM EGTA, 1 mM MgCl<sub>2</sub>) + 1 mM GTP for 15 min at 37°C and polymerized MTs were stabilized with 20 μM taxol (Sigma, T1912). MTs were centrifuged over a 25% sucrose cushion to remove aggregates and unassembled tubulin before use.

**Assembly of microtubule-axoneme crossings on reflective substrates.** Purified, fluorescently labeled sea urchin axonemes [Supplementary reference 12] were flowed onto silicon wafers and allowed to adhere for 10 min. After washing excess unbound axonemes using BRB80 buffer (80 mM Pipes pH 6.8, 2 mM MgCl<sub>2</sub>, 1 mM EGTA), the chip was coated twice with 5 mg/ml BSA-biotin (Thermo Scientific, 29130), washed with BRB80, coated with 0.5 mg/ml streptavidin (Vector Labs, SA-5000), and washed again with BRB80 plus 10 mM taxol. Polymerized microtubules were then added to the wafer and allowed to adhere for 5-10 min. Unbound microtubules were washed away using BRB80/taxol, and the wafer was then submerged in BRB80/10 μM taxol with an oxygen scavenging system [Supplementary reference 13] and inverted for imaging.

**Assembly of membrane interfaces on reflective substrates.** Assembly of membrane interfaces was performed according to published protocols [4], with the exception that 10x-his tagged FRB and 10x-his tagged FKBP were used in place of GFPuv. Expression and purification of

recombinant human FKBP12 [Supplementary reference 14] and the FRB domain of human FRAP [Supplementary reference 15] have been described. Giant unilamellar vesicles were allowed to interact with the bilayer for 30 min to 1 hr before inverting wafer for imaging.

**Modeling SAIM data in Chimera software.** SAIM models were generated using Chimera software [Supplementary reference 16]. For microtubule model, SAIM data was opened in chimera as a list of x,y,z-coordinates for each pixel and a microtubule was modeled as a cylinder with radius 25 along a spline fit through the coordinates. For membrane models, SAIM topography maps (.tif) were opened as planes and the “topography” command was used to create a surface.

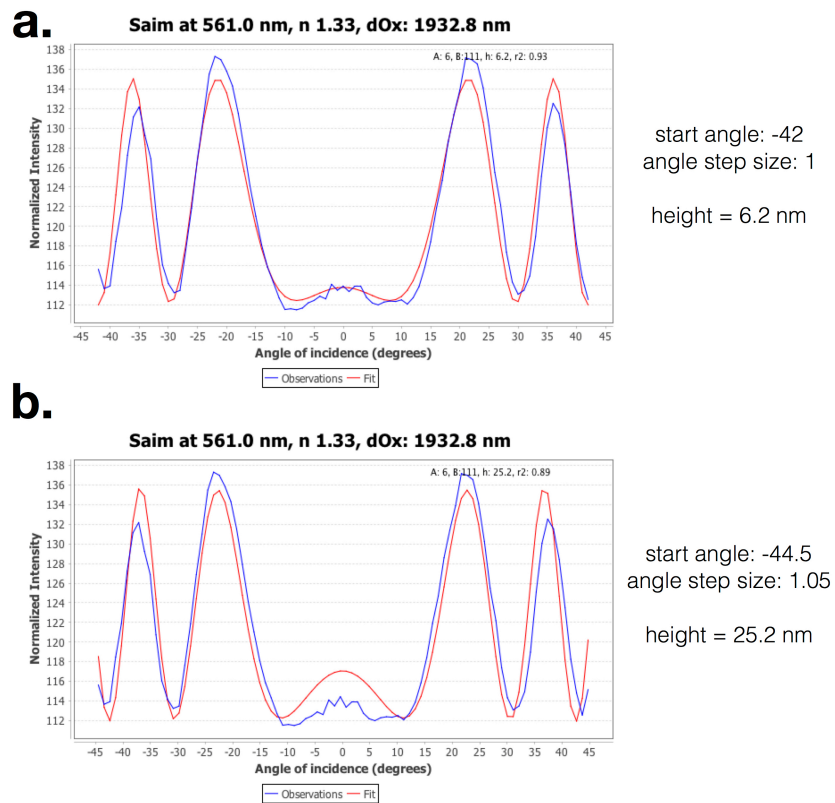
### Supplementary References

1. Paszek, M. J., DuFort, C. C., Rubashkin, M. G., Davidson, M. W., Thorn, K. S., Liphardt, J. T., & Weaver, V. M. (2012). Scanning angle interference microscopy reveals cell dynamics at the nanoscale. *Nature Methods*, 9(8), 825–827. doi:10.1038/nmeth.2077
2. Braun, D., & Fromherz, P. (1997). Fluorescence interference-contrast microscopy of cell adhesion on oxidized silicon. *Applied Physics A: Materials Science & Processing*, 65, 341–348. doi:10.1007/s003390050589
3. Lambacher, A., & Fromherz, P. (2002). Luminescence of dye molecules on oxidized silicon and fluorescence interference contrast microscopy of biomembranes. *Journal of the Optical Society of America B: Optical Physics*, 19(6), 1435–1453. doi:10.1364/JOSAB.19.001435

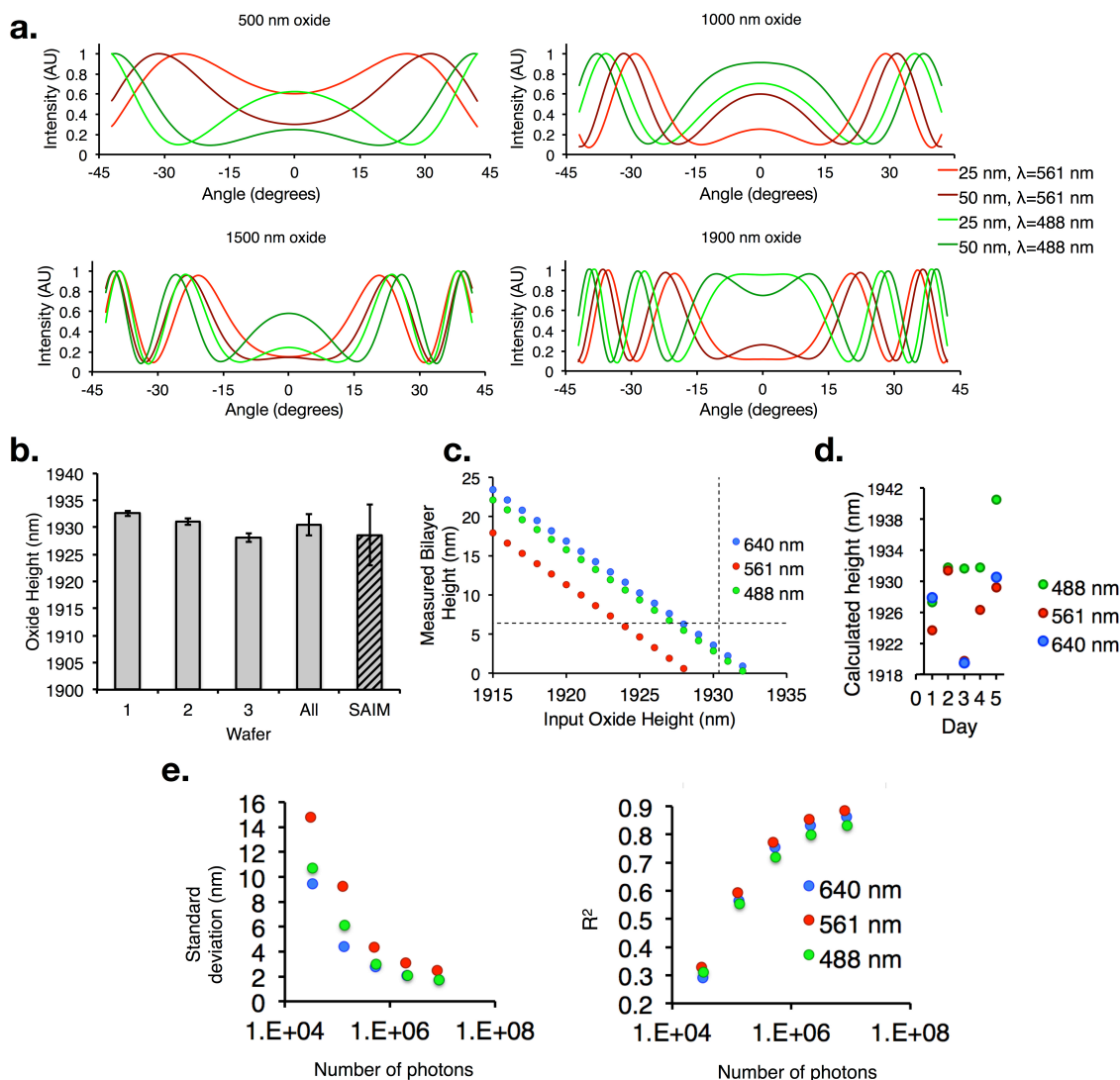
4. Ajo-Franklin, C. M., Ganesan, P. V., & Boxer, S. G. (2005). Variable incidence angle fluorescence interference contrast microscopy for z-imaging single objects. *Biophysical Journal*, *89*(4), 2759–69. doi:10.1529/biophysj.105.066738
5. Chung, M., Koo, B. J., & Boxer, S. G. (2013). Formation and analysis of topographical domains between lipid membranes tethered by DNA hybrids of different lengths. *Faraday Discuss.*, *161*, 333–345. doi:10.1039/C2FD20108A
6. Paszek, M. J., DuFort, C. C., Rossier, O., Bainer, R., Mouw, J. K., Godula, K., ... Weaver, V. M. (2014). The cancer glycocalyx mechanically primes integrin-mediated growth and survival. *Nature*, *511*(7509), 319–25. doi:10.1038/nature13535
7. Stehbens, S. J., Paszek, M., Pemble, H., Ettinger, A., Gierke, S., & Wittmann, T. (2014). CLASPs link focal-adhesion-associated microtubule capture to localized exocytosis and adhesion site turnover. *Nature Cell Biology*, *16*(6), 561–73. doi:10.1038/ncb2975
8. Liu, J., Wang, Y., Goh, W. I., Goh, H., Baird, M. A., Ruehland, S., ... Kanchanawong, P. (2015). Talin determines the nanoscale architecture of focal adhesions. *Proceedings of the National Academy of Sciences*, *112*(35), E4864–E4873. doi:10.1073/pnas.1512025112
9. Schneider, C. A., Rasband, W. S., & Eliceiri, K. W. (2012). NIH Image to ImageJ: 25 years of image analysis. *Nature Methods*, *9*(7), 671–5. doi:10.1038/nmeth.2089
10. Kučerka, N., Nieh, M.-P., & Katsaras, J. (2011). Fluid phase lipid areas and bilayer thicknesses of commonly used phosphatidylcholines as a function of temperature. *Biochimica et Biophysica Acta (BBA) - Biomembranes*, *1808*(11), 2761–2771. doi:10.1016/j.bbamem.2011.07.022

11. Castoldi, M., & Popov, A. V. (2003). Purification of brain tubulin through two cycles of polymerization–depolymerization in a high-molarity buffer. *Protein Expression and Purification*, 32(1), 83–88. doi:10.1016/S1046-5928(03)00218-3
12. Gibbons, I. R., & Fronk, E. (1979). A latent adenosine triphosphatase form of dynein 1 from sea urchin sperm flagella. *The Journal of Biological Chemistry*, 254(1), 187–96. pmid:214440
13. Aitken, C.E., R.A. Marshall, & J.D. Puglisi. (2008). An oxygen scavenging system for improvement of dye stability in single-molecule fluorescence experiments. *Biophys J.* 94:1826-1835. doi: 10.1529/biophysj.107.117689
14. Van Duyne, G. D., Standaert, R. F., Karplus, P. A., Schreiber, S. L., & Clardy, J. (1993). Atomic Structures of the Human Immunophilin FKBP-12 Complexes with FK506 and Rapamycin. *Journal of Molecular Biology*, 229(1), 105–124. <http://doi.org/10.1006/jmbi.1993.1012>
15. Chen, J., Zheng, X. F., Brown, E. J., & Schreiber, S. L. (1995). Identification of an 11-kDa FKBP12-rapamycin-binding domain within the 289-kDa FKBP12-rapamycin-associated protein and characterization of a critical serine residue. *Proceedings of the National Academy of Sciences of the United States of America*, 92(11), 4947–51. Retrieved from <http://www.ncbi.nlm.nih.gov/pubmed/7539137>
16. Pettersen, E. F., Goddard, T. D., Huang, C. C., Couch, G. S., Greenblatt, D. M., Meng, E. C., & Ferrin, T. E. (2004). UCSF Chimera—A visualization system for exploratory research and analysis. *Journal of Computational Chemistry*, 25(13), 1605–1612. doi:10.1002/jcc.20084

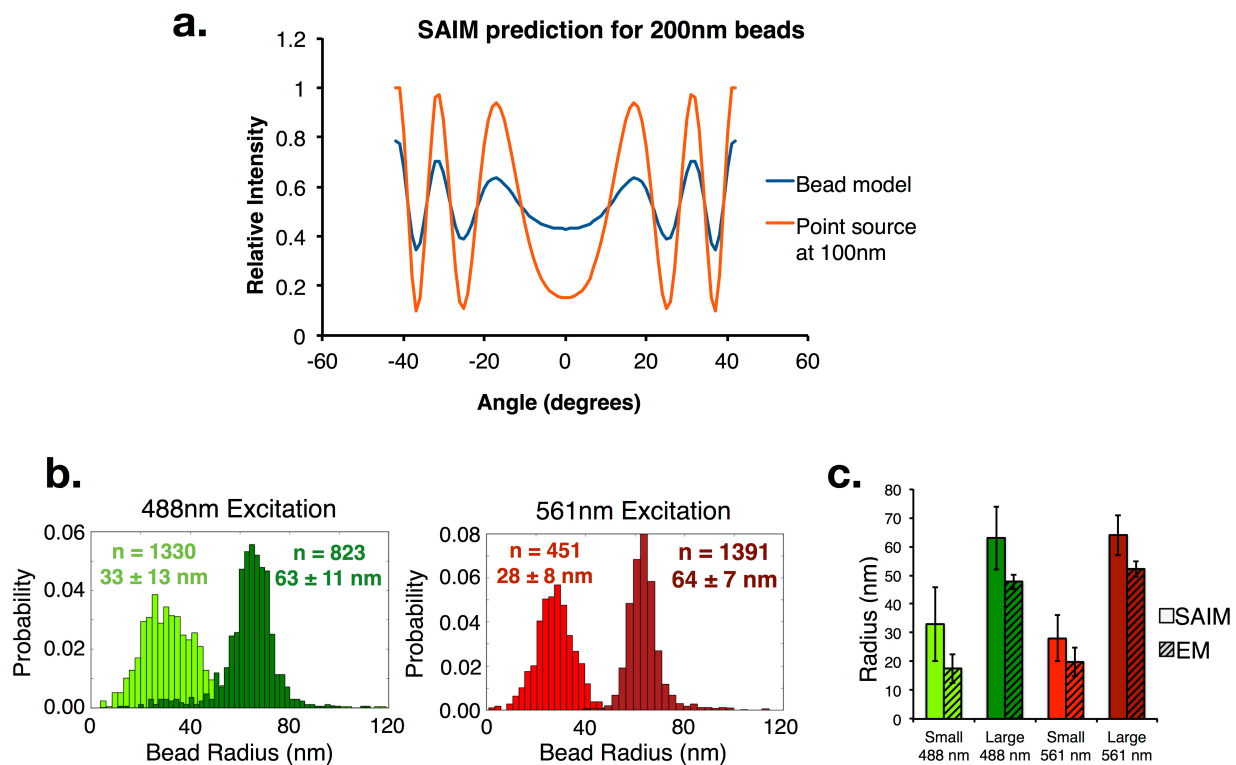




**Supplementary Figure 1.** Height error introduced by calibration error. **(a)** Correctly calibrated data. SAIM Data from a DiI labeled supported lipid bilayer fit correctly. Intensity measurements were taken at 1-degree intervals from  $-42^\circ$  to  $42^\circ$ . **(b)** Incorrectly calibrated data. The same data as in **a**, fit with a false calibration wherein the measurements were aligned to a start angle of  $-44.5^\circ$  and an angle step size of  $1.05^\circ$ .



**Supplementary Figure 2.** Calibration using supported lipid bilayers. **(a)** Periodicity of SAIM function at differing oxide heights. Theoretical intensity is plotted vs. angle for 488 nm (green lines) or 561 nm (red lines) laser illumination at 25 (light lines) nm or 50 nm (dark lines) from the surface of the oxide. Four oxide heights are represented: 500 nm, 1000 nm, 1500 nm and 1900 nm. **(b)** Measurement of oxide layer thickness. Three separate wafers were measured by ellipsometry at 8 positions spaced at increments of  $\sim 1$  cm apart. Error bars represent standard deviation of these eight measurements. “All” depicts the mean and standard deviation of 24 measurements across three wafers ( $1930.5 \pm 2.0$  nm). “SAIM” depicts the mean and standard deviation for the deduced oxide height at three wavelengths (488 nm, 561 nm, 647 nm), on two different microscopes and on five separate days ( $1928.5 \pm 5.6$  nm) for wafer #3. **(c)** Using SAIM to deduce oxide thickness. A triple labeled bilayer (DiO, DiI, DiD) was measured by SAIM at three wavelengths (488 nm, 561 nm, 647 nm). These data were then fit using oxide thicknesses ranging from 1915 nm to 1935 nm, which is plotted here versus the resultant sample height. Vertical dashed line represents the oxide thickness measured by ellipsometry ( $1930.5 \pm 2.0$  nm). Horizontal dashed line represents the expected height of the supported lipid bilayer (6.4 nm) [Supplementary reference 10]. Deduced oxide height is the intersection of the horizontal line for true bilayer height and the data. **(d)** Daily wavelength-dependent variation in oxide height measurements. Data for “SAIM” in **b** are shown as individual data points to highlight day-to-day variability.



**Supplementary Figure 3.** Imaging fluorescent nanobeads. (a) SAIM prediction for 200 nm fluorescent nano-sized beads. Model of the SAIM intensity function a 200nm sphere, stained throughout generated by dividing the sphere in 9 parts, calculating the SAIM curve for each part, and averaging the predicted intensity for the 9 parts at each angle (weighted by the fraction of the sphere's volume contained in each part) (blue line), compared to the SAIM curve of a point source at the radius of the bead (orange line). (b) Histogram of fluorescent nanobead radii measured by SAIM. Left, histogram of yellow-green nanobeads. Measured heights of nominal “20 nm” radius (company provided specifications) nanobeads shown in light green (n = 1330, mean = 33 ± 13 nm), and nominal “50 nm” radius nanobeads shown in dark green (n = 823, mean = 63 ± 11 nm). Right, histogram of red nanobeads. Measured heights of nominal 20 nm radius nanobeads shown in light red (n = 451, mean = 28 ± 8 nm), and nominal 50 nm radius nanobeads shown in dark red (n = 1391, mean = 64 ± 7 nm). (c) Comparison of nanobead radius measured by SAIM or electron microscopy. Color-coding corresponds to panel b, radii measured by SAIM are solid colored, radii measured by electron microscopy are indicated by hatch marks. Error bars denote standard deviation.

## 2.6 Author Contributions

C.B.C., R.D.V., and N.S. designed the research; N.S. and C.B.C. developed the software and calibration device; C.B.C. collected data to test software; C.B.C. and N.S. drafted the article; C.B.C., R.D.V., and N.S. edited the article; and all authors read and approved the final article.

## 2.7 Acknowledgements

We would like to thank G. Bhabha and S. Niekamp for help with electron microscopy, axoneme and microtubule experiments and J. Sung and S. Vo (director of the Leia3d Advance Lithography Center in Palo Alto, California) for ellipsometry measurements. We thank T. Goddard and E. Meng for help generating topography models of SAIM data using Chimera software. We are grateful to V. Weaver and M. Rubashkin for initial help implementing SAIM and to M. Paszek and W. Shin for useful discussions about the SAIM software and calibration device. We thank G. Bhabha and A. Jain for comments on the manuscript. The authors acknowledge funding from the National Institutes of Health (R01EB007187, R.D.V.) and the Howard Hughes Medical Institute.

## 2.8 References

31. Lambacher, A., & Fromherz, P. (1996). Fluorescence interference-contrast microscopy on oxidized silicon using a monomolecular dye layer. *Applied Physics A: Materials Science & Processing*, 63(3), 207–216. doi:10.1007/s003390050374
32. Ajo-Franklin, C. M., Ganesan, P. V, & Boxer, S. G. (2005). Variable incidence angle fluorescence interference contrast microscopy for z-imaging single objects.

- Biophysical Journal*, 89(4), 2759–69. doi:10.1529/biophysj.105.066738
33. DuFort, Christopher, Paszek, M. (2014). Nanoscale cellular imaging with scanning angle interference microscopy. *Methods Cell Biol.*, 123, 235–52.  
<http://doi.org/10.1016/B978-0-12-420138-5.00013-6>
34. Edelstein, A., Amodaj, N., Hoover, K., Vale, R. & Stuurman, N. (2010). Computer Control of Microscopes Using  $\mu$ Manager. In *Current Protocols in Molecular Biology* (eds. Ausubel, F.M. et al.) Unit 14.20 (Hoboken, NJ, USA: John Wiley & Sons, Inc. doi:10.1002/0471142727.mb1420s92).
35. Schindelin, J., Arganda-Carreras, I., Frise, E., Kaynig, V., Longair, M., Pietzsch, T., ... Cardona, A. (2012). Fiji: an open-source platform for biological-image analysis. *Nature Methods*, 9(7), 676–82. doi:10.1038/nmeth.2019
36. Schmid, E. M., Bakalar, M. H., Choudhuri, K., Weichsel, J., Ann, H. S., Geissler, P. L., ... Fletcher, D. A. (2016). Size-dependent protein segregation at membrane interfaces. *Nature Physics*, 12(7), 704–711. <http://doi.org/10.1038/nphys3678>

## CHAPTER 3

# ***In vitro* reconstitution of T cell receptor-mediated segregation of the CD45 phosphatase**

Catherine B. Carbone<sup>1</sup>, Nadja Kern<sup>1</sup>, Ricardo A. Fernandes<sup>2</sup>, Enfu Hui<sup>1</sup>, Xiaolei Su<sup>1</sup>, K. Christopher Garcia<sup>2</sup>, and Ronald D. Vale<sup>1</sup>

<sup>1</sup>Dept. of Cellular and Molecular Pharmacology and the Howard Hughes Medical Institute, University of California, San Francisco, CA 94158; <sup>2</sup>Dept. of Molecular and Cellular Physiology and Structural Biology and the Howard Hughes Medical Institute, Stanford University Medical School, CA 94305

### **3.1 Significance**

The T cell receptor (TCR) and PD-1 signaling cascades have been hypothesized to be triggered by the exclusion of the transmembrane phosphatase CD45 from sites of receptor–ligand engagement at the T cell–antigen-presenting cell interface. We reconstituted TCR–pMHC– and PD1–PD-L1–mediated segregation of CD45 with purified proteins and model membranes, demonstrating that this phenomenon can occur in the absence of any active cellular organization. In this minimal system, two developmentally regulated and different size isoforms of CD45 are differently segregated by TCR–pMHC binding, suggesting a possible mechanism for the fine-tuning of signaling. Collectively, our data show that the binding energy of physiological receptor–ligand pairs is sufficient to create spatial organization in membranes.

### **3.2 Abstract**

T cell signaling initiates upon the binding of peptide-loaded MHC (pMHC) on an antigen-presenting cell to the T cell receptor (TCR) on a T cell. TCR phosphorylation in response to pMHC binding is accompanied by segregation of the transmembrane phosphatase CD45 away from TCR–pMHC complexes. The kinetic segregation hypothesis proposes that CD45 exclusion shifts the local kinase–phosphatase balance to favor TCR phosphorylation. Spatial partitioning may arise from the size difference between the large CD45 extracellular domain and the smaller TCR–pMHC complex, although parsing potential contributions of extracellular protein size, actin activity, and lipid domains is difficult in living cells. Here, we reconstitute segregation of CD45 from bound receptor–ligand pairs using purified proteins on model membranes. Using a model receptor–ligand pair (FRB–FKBP), we first test physical and computational predictions for protein organization at membrane interfaces. We then show that the TCR–pMHC interaction

causes partial exclusion of CD45. Comparing two developmentally regulated isoforms of CD45, the larger RABC variant is excluded more rapidly and efficiently (~50%) than the smaller R0 isoform (~20%), suggesting that CD45 isotypes could regulate signaling thresholds in different T cell subtypes. Similar to the sensitivity of T cell signaling, TCR–pMHC interactions with Kds of  $\leq 15 \mu\text{M}$  were needed to exclude CD45. We further show that the coreceptor PD-1 with its ligand PD-L1, immunotherapy targets that inhibit T cell signaling, also exclude CD45. These results demonstrate that the binding energies of physiological receptor–ligand pairs on the T cell are sufficient to create spatial organization at membrane–membrane interfaces.

### 3.3 Introduction

Binding of the T cell receptor (TCR) to agonist peptide-MHC (pMHC) triggers a signaling cascade within a T cell leading to reorganization of the cytoskeleton and organelles, transcriptional changes, and cell proliferation. The first step in the cascade is TCR phosphorylation by the Src family tyrosine kinase Lck (2). One model, called “kinetic segregation” (3) for how this initiating phosphorylation is triggered, proposes that the close membrane contact created by TCR–pMHC binding results in exclusion of the transmembrane phosphatase CD45, and the shift of the kinase–phosphatase balance favors net phosphorylation of the TCR by Lck. The basis of this exclusion is thought to be steric, since the large CD45 extracellular domain (CD45 R0 isoform, 25 nm; CD45 RABC isoform, 40 nm) (Table S1) (4–6) may not be able to penetrate the narrow intermembrane spacing generated by the TCR–pMHC complex (13 nm) (Table S1) (7, 8).



Imaging T cells activated *ex vivo* either by B cells (9) or by antigen presented on supported lipid bilayers (SLBs) (10, 11) has revealed that CD45 is indeed partitioned away from the TCR upon pMHC binding. Cellular reconstitutions have demonstrated that the large extracellular domain of CD45 is required for this segregation (12, 13). Additionally, size-dependent segregation of CD45 by orthogonal receptor–ligand pairs that create a similar narrow intermembrane cleft is sufficient for T cell triggering in the absence of TCR–pMHC binding (6, 12).

Despite this strong cellular evidence for size-based partitioning, it has been debated whether the physical properties of CD45 and TCR–pMHC at the membrane–membrane interface alone are sufficient to explain the observed segregation behavior or whether other cellular factors (e.g., actin cytoskeletal or lipid ordering) are also required. Several groups have computationally modeled aspects of size-based organization at membrane interfaces, and two independent mathematical approaches have concluded that spontaneous pattern formation can occur in physiological parameter ranges (14, 15). These models predict the contributions of protein (size, concentration, elasticity, affinity, and kinetics), membrane (stiffness, tension, repulsion), and environmental (thermal fluctuations, cytoskeleton, time) factors in regulating partitioning. Although these models focus primarily on a system with two binding pairs (TCR–pMHC and ICAM-1–LFA-1), some of the predictions can be extrapolated to a system with both ligand-bound and unbound species.

Successful efforts to reconstitute molecular segregation at membrane–membrane interfaces have been made with dimerizing GFP molecules (16) and hybridizing strands of DNA (17). These studies show that laterally mobile molecules at membrane–membrane interfaces organize by

height and locally deform the membrane to accommodate different molecular sizes. However, results from high-affinity, artificial receptor–ligand pairs cannot be simply extrapolated to predict results for physiologically relevant molecules at the T cell–APC interface. Here, we have recapitulated TCR–pMHC–mediated partitioning of CD45 on model membranes.

### 3.4 Results

#### **A chemically-inducible receptor-ligand system for producing CD45 exclusion at a membrane-membrane interface**

To mimic a T cell, we used a giant unilamellar vesicle (GUV) containing a nickel-chelating lipid to which a purified His-tagged, fluorescently-labeled receptor and CD45 could be added (**Fig. 1A**). To mimic the APC, we used a supported lipid bilayer (SLB) containing nickel-chelating lipids to which a His-tagged protein ligand also could be bound. All proteins were linked to their target membrane via either His<sub>10</sub> or His<sub>12</sub>, as detailed in the methods section. As an initial test of this system, we used an artificial receptor (FKBP) and ligand (FRB) that could be induced to form a tight binding interaction (100 fM) upon addition of rapamycin (17). In order to maintain the GUV and SLB in proximity prior to rapamycin addition, the two membranes were passively tethered to one another using two 100-mer single-stranded DNA molecules with a 20 bp region of complementarity (18, 19) (**Table S1**). The elongated extracellular domain of the CD45 R<sub>0</sub> isoform (25 nm) (3–5) or the smaller SNAP protein (5 nm, **Table S1**) (20) were used as test proteins for partitioning.

Upon rapamycin addition, FKBP and FRB concentrated first in small micron-scale clusters at the GUV-SLB interface, which then grew in size over the interface; simultaneously, fluorescently-

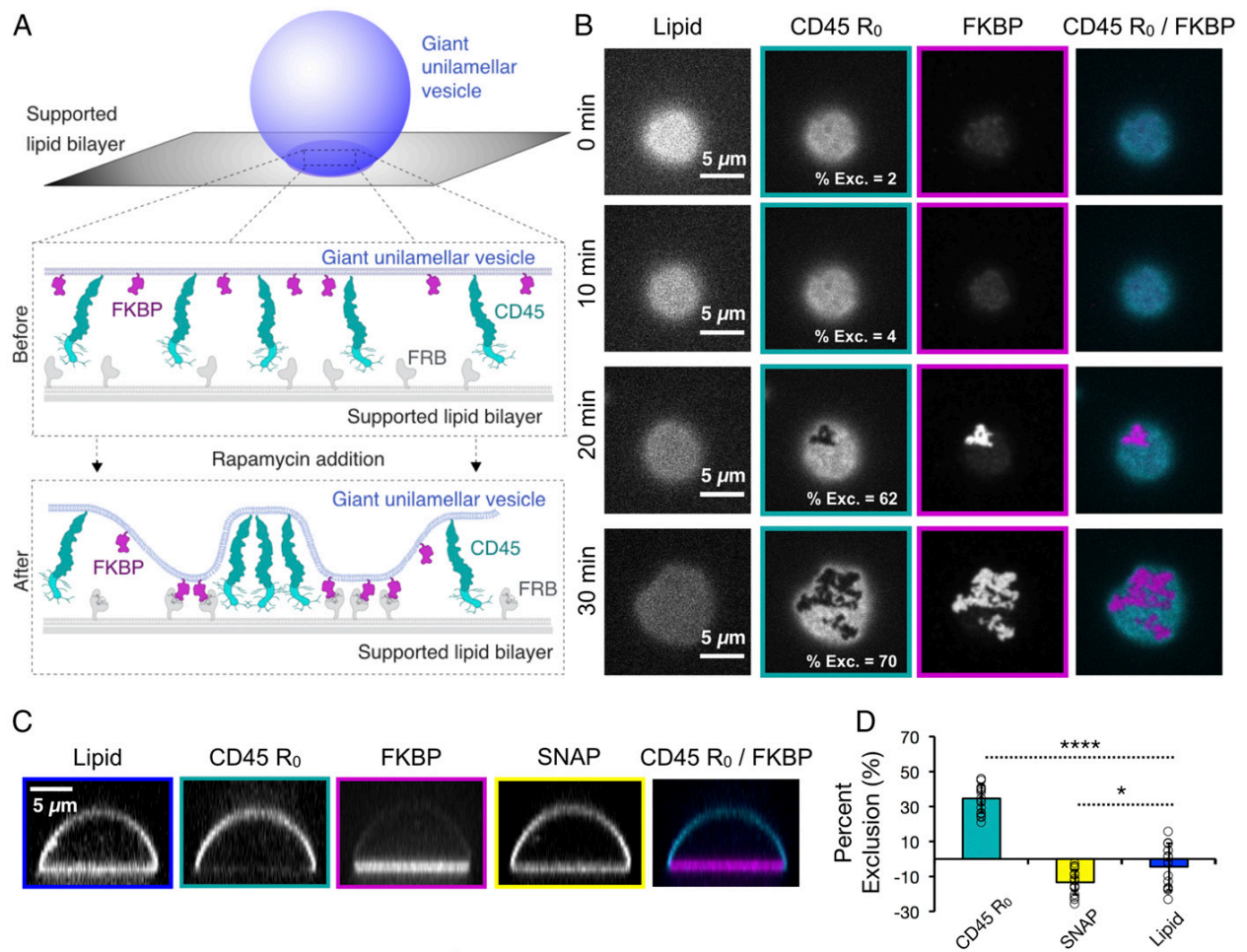


**Fig. 1.** Receptor-ligand binding induces CD45 segregation at membrane interfaces. **(A)** Schematic of rapamycin-induced receptor (FKBP)-ligand (FRB) binding and CD45 R<sub>0</sub> segregation between a giant unilamellar vesicle (GUV) and a supported lipid bilayer (SLB) **(B)** Total internal reflection fluorescence (TIRF) microscopy of a GUV-SLB interface at indicated times after rapamycin addition, showing concentration of FKBP into microdomains that exclude CD45 R<sub>0</sub>. Percent exclusion of CD45 R<sub>0</sub> is indicated for each image shown. **(C)** Spinning disk z-sections of GUVs after membrane-apposed interfaces have reached equilibrium, showing localization of FKBP to the membrane interface, localization of CD45 R<sub>0</sub> away from the interface, and uniform distribution of SNAP. **(D)** Quantification of experiment shown in C; mean  $\pm$  standard deviation (n=17 GUVs pooled from two experiments).

labeled CD45 R<sub>0</sub> partitioned away from regions of the GUV that became enriched in receptor-ligand (**Fig. 1B and Movie S1**). In contrast to CD45, which was strongly depleted by FRB-FKBP, the SNAP protein (5 nm) (21) or a lipid dye (Atto390-DOPE) remained evenly distributed throughout the interface after rapamycin addition (**Fig. 1C-D**). We also tested PD-L1 (8 nm, **Table S1**), which also remained evenly distributed throughout the interface after rapamycin addition (**Fig. S1**). The size of FKBP-FRB clusters could be varied by changing the receptor concentration on the GUV membrane; however, the degree of CD45 R<sub>0</sub> exclusion from clusters was similar over the range tested (**Fig. 2A-C**). Across all concentrations of FKBP, at receptor-ligand enriched zones, CD45 R<sub>0</sub> was depleted by  $72 \pm 7\%$  (n=22 GUVs pooled from two experiments). Once formed, the receptor -enriched and -depleted zones stably retained their shapes for tens of minutes and receptor-ligand pairs in the enriched zones were largely immobile, as evidenced by fluorescence recovery after photobleaching (FRAP; **Fig. S2**). However, using single molecule TIRF imaging, we observed that single molecules of CD45 R<sub>0</sub> can diffuse across FKBP-FRB -enriched and -depleted zones (**Fig. 2D-E, Movie S2**). This result reveals that individual molecules can exchange across these micron-scale boundaries.

In addition to testing the CD45 R<sub>0</sub> isoform for segregation, we also compared the extracellular domain of the CD45 R<sub>ABC</sub> isoform, which is preferentially expressed early in T cell development (22), and is about 15 nm larger in size than the shorter and later expressed R<sub>0</sub> isoform (**Table S1**) (3, 4). With both isoforms present on the same GUV, the larger CD45 R<sub>ABC</sub> isoform segregated from newly forming FKBP clusters three-fold faster than the R<sub>0</sub> isoform ( $2.8 \pm 0.9$ -fold, n=7 GUVs pooled from two experiments, **Fig. 2F-G, Movie S3**). However, the final extent of

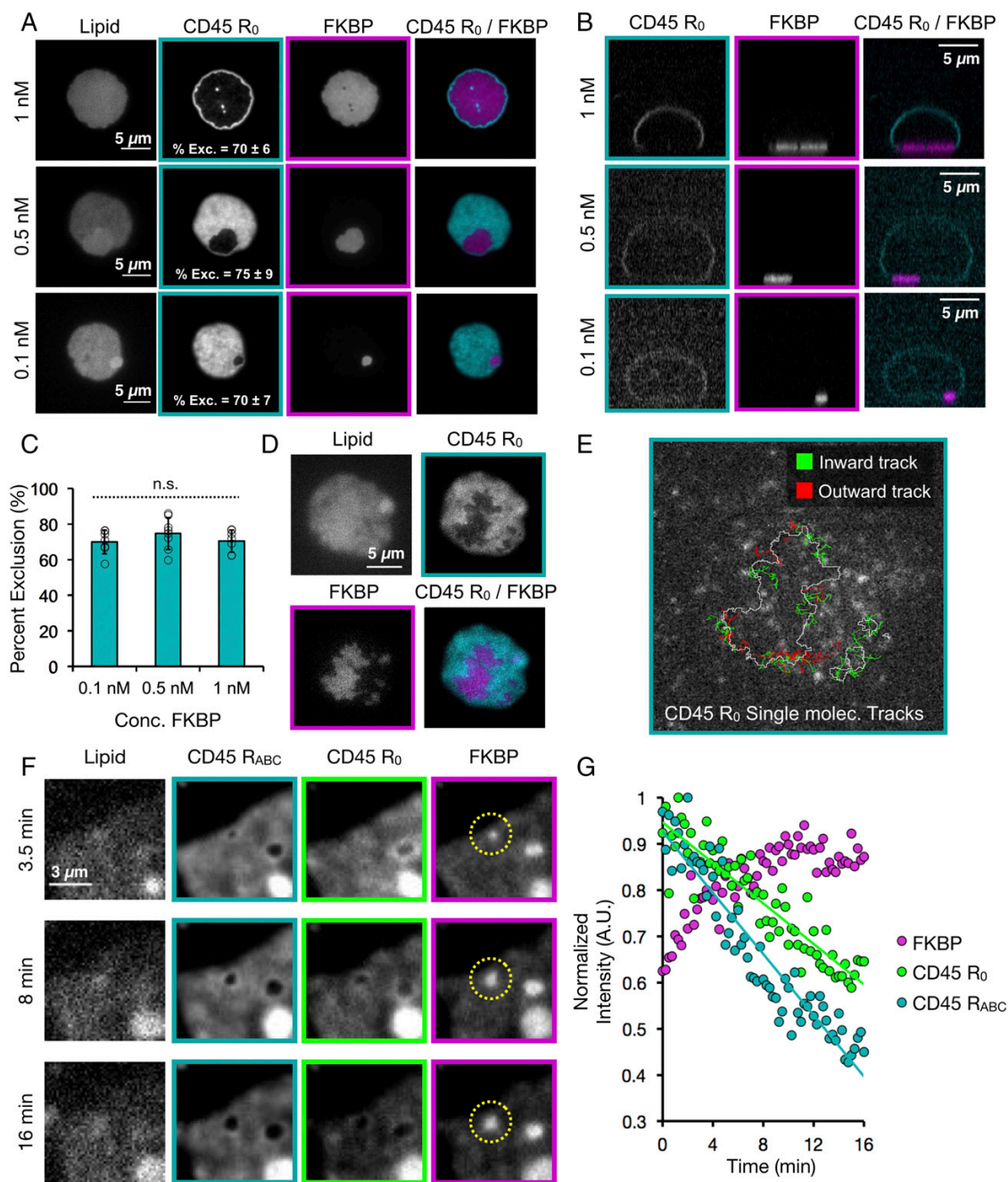


**Fig. 2.** Characterization of partitioned GUV-SLB membrane-membrane interfaces. **(A)** Titration of FKBP concentration (indicated at left of images) with constant CD45 R<sub>0</sub> concentration imaged by TIRF microscopy. Percent exclusion of CD45 R<sub>0</sub> is indicated as mean ± standard deviation with n=7-8 GUVs per condition pooled from three experiments. **(B)** Spinning disk z-sections of GUVs shown in **A**. **(C)** Graphical representation of data shown in **A**. **(D)** Total internal reflection fluorescence (TIRF) microscopy of a GUV-SLB interface showing overall localization of CD45 R<sub>0</sub> and FKBP. **(E)** Single molecule imaging of CD45 R<sub>0</sub> for GUV shown in **D**, border of FKBP enriched zone indicated by white line. Only tracks crossing the exclusion boundary are shown. CD45 R<sub>0</sub> single molecule tracks originating outside FKBP enriched zone are shown as green lines and tracks originating inside the FKBP enriched zone are shown as red lines. **(F)** Total internal reflection fluorescence (TIRF) microscopy of a GUV-SLB interface at 30-sec time points after rapamycin addition showing concentration of FKBP into micro domains that exclude CD45 R<sub>0</sub> and CD45 R<sub>ABC</sub>. Rate of CD45 R<sub>ABC</sub> exclusion is  $2.8 \pm 0.9$  times faster than rate of CD45 R<sub>0</sub> exclusion, n=7 GUVs from two experiments. **(G)** Quantification of exclusion for representative GUV shown in **F**.

exclusion between the two CD45 isoforms was similar with this high affinity FRB-FKBP system (**Fig. S3**).

The kinetic segregation model predicts that CD45 is excluded from receptor-ligand complexes based upon a difference in the spacing between the GUV and SLB in the receptor- versus CD45-enriched regions (2). To investigate the topology of the GUV membrane across the interface with nanometer accuracy in the vertical axis, we used scanning angle interference microscopy (SAIM), a technique that calculates the distance of fluorophores from a silicon oxide wafer by collecting sequential images at multiple illumination angles (**Fig. 3A**) (23). The SAIM reconstructions revealed membrane deformations at regions of CD45 localization (**Fig. 3B-D**). The calculated difference in membrane spacing between the FRB-FKBP- and CD45 R<sub>0</sub>- enriched regions was  $18 \pm 11$  nm (n=4-6 regions from each of 4 GUVs from two experiments, pooled), suggesting a size of ~24 nm for the CD45 R<sub>0</sub> extracellular domain, assuming that FRB-FKBP creates an intermembrane space of 6 nm (**Table S1**) (24). This value is similar to the ~22 nm axial dimension for the CD45 R<sub>0</sub> extracellular domain determined by electron microscopy (5). Conversely, for GUV-SLB interfaces with FRB-FKBP and SNAP, SAIM reconstructions revealed no changes in membrane spacing across the GUV-SLB interface (**Fig. 3E-G**).

### **TCR-pMHC –mediated CD45 exclusion**

Next, we sought to establish a GUV-SLB interface using the native T cell receptor-ligand pair, TCR-pMHC (**Fig. 4A**). For the TCR, we co-expressed the extracellular domains of the 2B4  $\alpha$  and  $\beta$  chains extended with leucine zippers to stabilize their dimerization (25); both chains were tagged with His<sub>10</sub> for conjugation to the GUV membrane and the  $\beta$  chain contained a ybbR

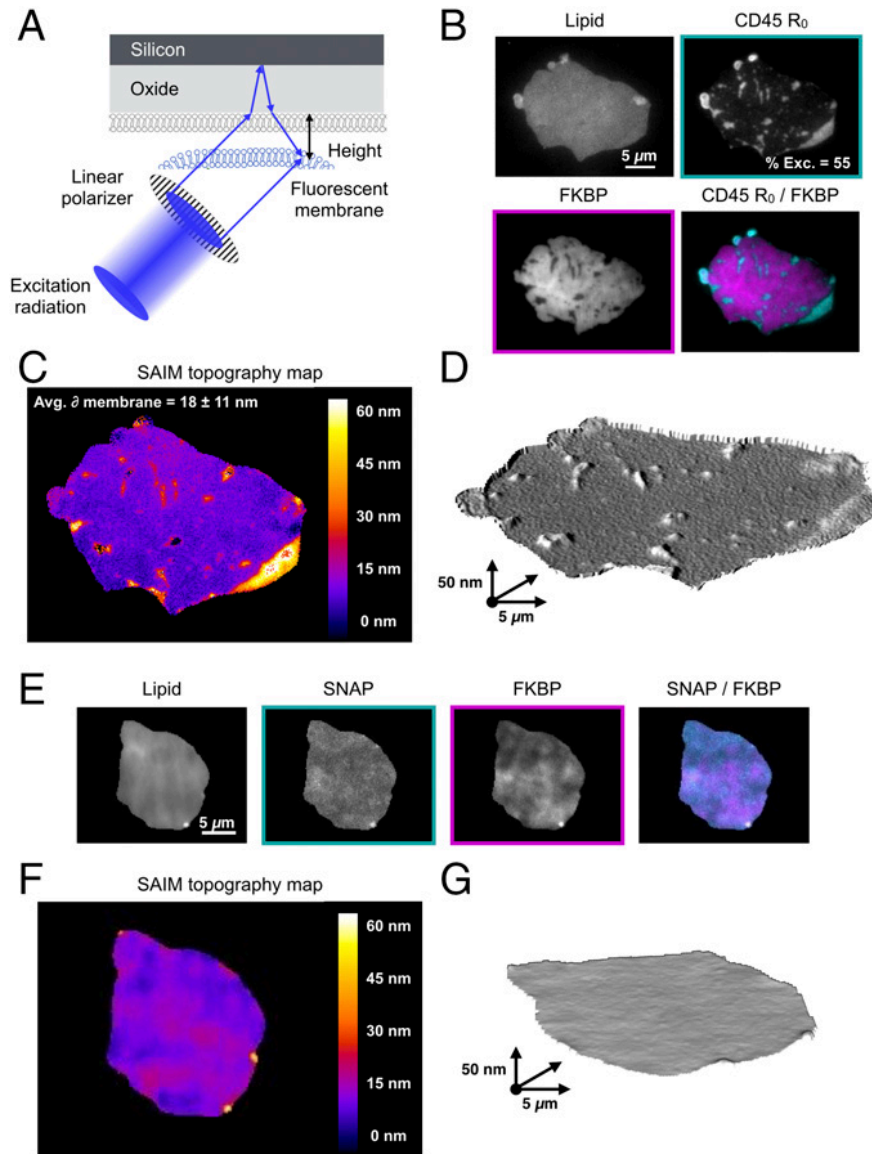


**Fig. 3.** Membrane topology is influenced by local protein composition. (A) Schematic of scanning angle interference microscopy showing reflection and interference of excitation light that produces structured illumination patterns used to deduce fluorophore height; adapted from Carbone, et al., 2016. (B) Epifluorescence microscopy showing localization of lipid, CD45 R<sub>0</sub> and FKBP on GUV analyzed by SAIM imaging. Percent exclusion of CD45 R<sub>0</sub> indicated for image shown. (C) SAIM reconstruction of GUV membrane derived from lipid fluorescence showing an increase in membrane height at CD45 R<sub>0</sub> clusters. Average membrane height change depicted as mean  $\pm$  standard deviation, n=4-6 clusters from each of 4 GUVs imaged during two separate experiments. (D) 3D model of data shown in c. Z-scale is exaggerated to clearly depict membrane deformations. (E) Epifluorescence microscopy showing localization of lipid, SNAP, and FKBP on GUV analyzed by SAIM imaging. (F) SAIM reconstruction of GUV membrane derived from lipid fluorescence (G) 3D model of data shown in F. Z-scale is exaggerated to clearly depict membrane deformations.

peptide for fluorescent labeling. For the ligand, we used the IE<sup>k</sup> MHC, His<sub>10</sub>-tagged loaded with a high affinity (2.5 μM Kd) peptide. Similar to the results previously described for FRB-FKBP, we observed the formation of micron-sized TCR clusters that excluded CD45 R<sub>0</sub> (22 ±14% exclusion, n=17 GUVs pooled from 2 experiments, **Fig. 4B**) but not the control SNAP domain (**Fig. S3A**).

We also combined both CD45 R<sub>ABC</sub> and CD45 R<sub>0</sub> isoforms on the same GUV and compared their segregation with the TCR-pMHC system. Upon GUV contact with the SLB, the 2B4 TCR bound the IE<sup>k</sup> MHC, and concentrated at the interface where it formed micron-scale clusters that excluded both isoforms of CD45 (**Fig. 4C**). However, unlike the high affinity FKBP-FRB system in which the two CD45 isoforms R<sub>0</sub> and R<sub>ABC</sub> are excluded to a similar level (Fig. S3), the degree of TCR-pMHC mediated exclusion of the smaller CD45 R<sub>0</sub> isoform (15 ± 7% exclusion) was lower than the larger CD45 R<sub>ABC</sub> isoform (38 ± 9% exclusion) at steady state (45 min, n=13 GUVs pooled from two experiments, **Fig. 4D**).

*In vivo*, TCR encounters MHCs loaded with a myriad of different peptides; although not absolute, TCR-pMHC affinities of <50 μM are usually required to trigger a signaling response (26). To examine the effect of TCR-pMHC affinity on CD45 R<sub>ABC</sub> exclusion, we loaded IE<sup>k</sup> MHC with a series of well-characterized peptides with resultant two dimensional Kds of 2.5 μM, 7.7 μM, 15 μM, 50 μM and null for the 2B4 TCR (25). At steady state, we observed that pMHCs with affinities to the TCR of 15 μM and lower excluded CD45 R<sub>ABC</sub> to similar extents (51 ± 7% exclusion, n=30 GUVs pooled from two experiments, **Fig. 4E-F**). However, the pMHC with a Kd of 50 μM and IE<sup>k</sup> loaded with null peptides did not concentrate TCR at the GUV-SLB



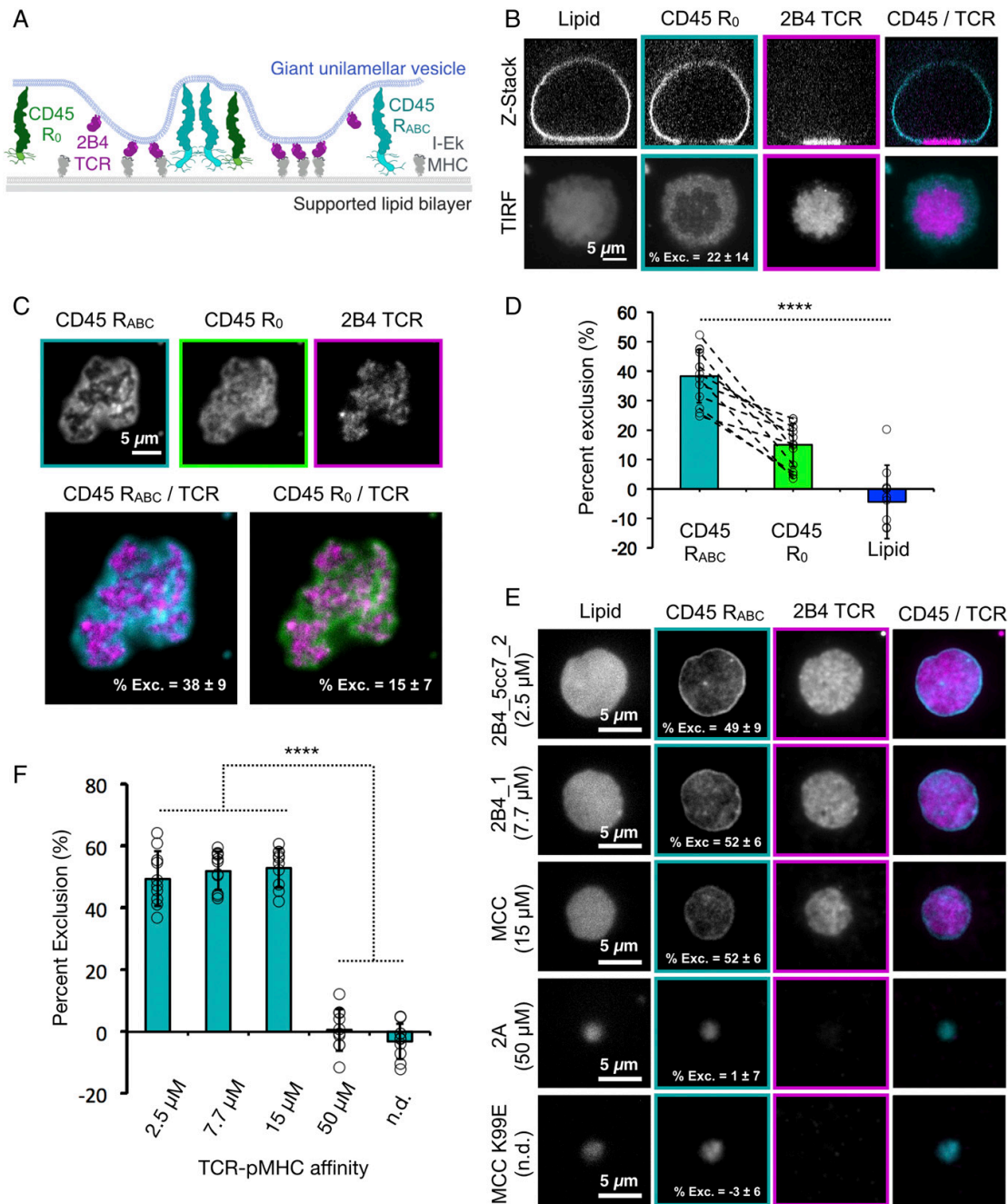


**Fig. 4.** TCR-pMHC binding induces CD45 segregation at GUV-SLB interfaces (A) Schematic of 2B4 TCR-IE<sup>k</sup> MHC binding between a GUV and a SLB, and segregating away from two CD45 isoforms (R<sub>0</sub> and R<sub>ABC</sub>). (B) Top, spinning disk z-sections of GUVs after membrane-apposed interfaces have reached equilibrium, showing localization of 2B4 TCR to membrane interface and exclusion CD45 R<sub>0</sub> away from the interface. Bottom, TIRF images of GUV-SLB interface for GUV shown in panel above. Percent exclusion of CD45 R<sub>0</sub> indicated for image shown. (C) Top, segregation of CD45 R<sub>0</sub> and CD45 R<sub>ABC</sub> on the same GUV membrane away from 2B4 TCR, shown by TIRF microscopy of membrane interface. Percent exclusion of CD45 isoforms indicated as mean ± standard deviation, with n=13 GUVs from two experiments. (D) Graphical representation of data shown in C. (E) Dependence of CD45 R<sub>ABC</sub> exclusion as a function of TCR-pMHC affinity using peptides with different K<sub>d</sub>s, indicated at left of images. Imaged by TIRF microscopy of membrane interfaces. Percent exclusion of CD45 R<sub>ABC</sub> indicated as mean ± standard deviation, n=10 GUVs per condition from two experiments. (F) Graphical representation of data shown in E.

interface and did not change the distribution of CD45  $R_{ABC}$  ( $-1 \pm 6\%$  exclusion,  $n=20$  GUVs pooled from 2 experiments, **Fig. 4E-F**). Thus, in agreement with computational predictions (14), CD45  $R_{ABC}$  exclusion was observed over the same range of affinities that are associated with peptide agonists.

### **Exclusion of CD45 by PD-1 –PD-L1**

T cell signaling involves many receptor-ligand pairs interacting across the two membranes in addition to the TCR-pMHC (27). The co-receptor PD-1 and its ligand PD-L1 create a signaling system that opposes T cell activation by inhibiting CD28 signaling (28, 29). PD-1 ligation also results in microcluster formation on T cells (30). Like the TCR, PD-1 signaling is initiated through receptor tail phosphorylation by Lck (31), and this phosphorylation event may be opposed by the abundant CD45 phosphatase (**Fig. S4A-B**). Therefore we tested the ability of interaction of PD-1 with PD-L1, which forms a complex of similar dimension (9 nm) to TCR-pMHC (**Table S1**) (32) to partition CD45 in our in vitro liposome system (**Fig. 5A**). As expected from these physical dimensions, PD-1-PD-L1 interaction at the membrane-membrane interfaces formed micron-sized clusters that excluded CD45  $R_{ABC}$  (**Fig. 5B**). The degree of CD45  $R_{ABC}$  exclusion ( $60 \pm 14\%$  exclusion,  $n=14$  GUVs from two experiments **Fig. 5B**) was greater than that observed for TCR-pMHC (2.5  $\mu$ M peptide), which may be explained by the higher affinity of the PD1-PD-L1 interaction (0.77  $\mu$ M) (33).

We also combined CD45  $R_{ABC}$  with both TCR-pMHC with PD-1-PD-L1. In this dual receptor-ligand system, the two receptor-ligand complexes co-localized and CD45  $R_{ABC}$  was partitioned away from the combined ligated TCR-PD-1 footprint (**Fig. 5C**). The size (**Table S1**) and affinity

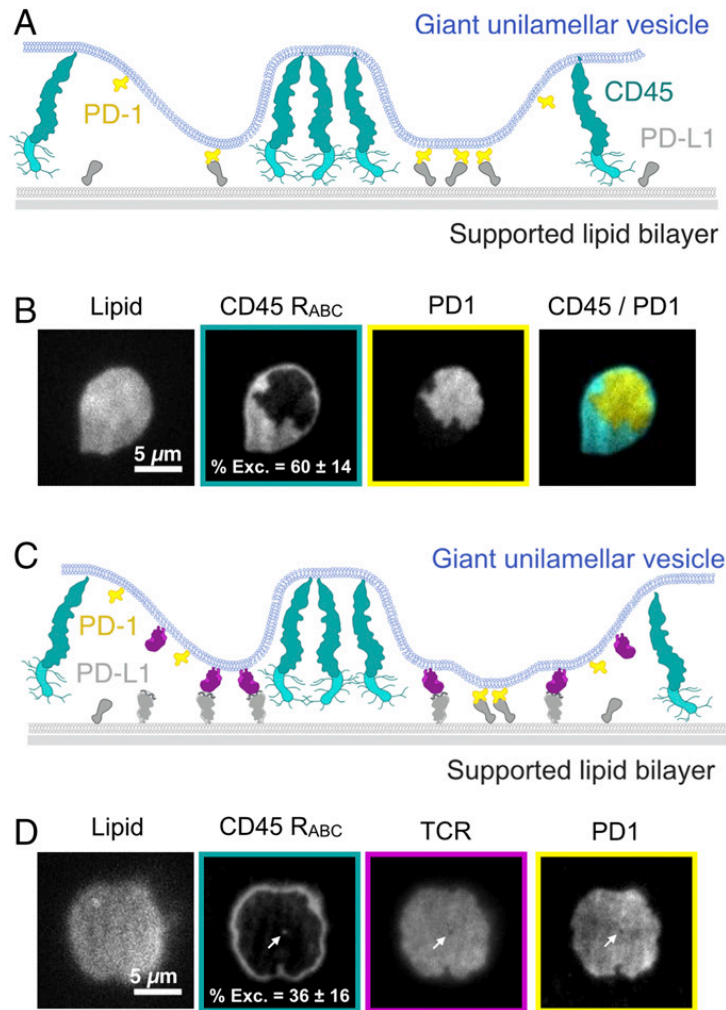


**Fig. 5.** The inhibitory co-receptor PD-1 excludes CD45 and colocalizes with TCR. (A) Schematic of PD-1-PD-L1 binding between a GUV and a SLB, with segregation away from CD45 R<sub>ABC</sub>. (B) TIRF microscopy showing concentration of PD-1 into microdomains that exclude CD45 R<sub>ABC</sub>. Percent exclusion of CD45 R<sub>ABC</sub> indicated as mean  $\pm$  standard deviation, n=14 GUVs from two experiments. (C) TIRF microscopy showing concentration of TCR and PD-1 into a domain that excludes CD45 R<sub>ABC</sub>. Percent exclusion of CD45 R<sub>ABC</sub> indicated as mean  $\pm$  standard deviation, n=14 GUVs from two experiments. White arrow highlights small CD45 R<sub>ABC</sub> enriched zone that is depleted for TCR and PD-1.

difference between TCR-pMHC and PD-1-PD-L1 may be small enough to not cause partitioning of these receptor-ligands under the conditions tested in our *in vitro* assay.

### **3.5 Discussion**

In this study, we have established an *in vitro* membrane system that recapitulates receptor-ligand mediated CD45 exclusion. We have found that the binding energy of physiological receptor-ligand interactions is sufficient for CD45 partitioning at a model membrane-membrane interface. We also show that subtle differences in sizes and affinities of the proteins at the interface can give rise to significant changes in spatial organization and discuss the implications of these findings in more detail below.

Spatial organization of TCR and CD45 at the immune cell contacts has been proposed to arise by a nucleation-spreading mechanism (14). By imaging an inducible synthetic receptor-ligand binding interaction in real time, we also conclude that pattern formation arises by the nucleation of small clusters that further spread across the membrane interface over time. These patterns induce changes in membrane topology that reflect the local protein composition and are stable on the order of hours. However, we show that individual molecules can freely exchange between domains. This result is consistent with previous computational simulations, although these models predict patterns will relax to a circular geometry to minimize the length of the domain boundaries (14, 34, 35). In our system, as observed for other physical models of partitioning using DNA-DNA hybridization (16) and dimerizing GFP (15), patterns have more complex domain structures. The lack of circular geometry in the experimental systems could be due to small inhomogeneities in the supported lipid bilayer compared to perfectly diffusive

computational models. Despite this difference, many physical and computational model systems have converged on nucleation and spreading as a general mechanism by which spatial organization arises at membrane-membrane interfaces.

The mechanism by which receptor-ligand binding induces spatial organization is a subject of active investigation. Our results showing differential exclusion of CD45 R<sub>0</sub> and CD45 R<sub>ABC</sub> indicate that size-based steric exclusion and membrane deformation are important for exclusion. In addition, protein crowding of receptor-ligand complexes also could provide a driving force for partitioning. Indeed, previous work has shown that patterns formed at analogous membrane-membrane interfaces using dimerizing GFP as the receptor-ligand pair and a small test protein (monomeric Cherry) are due to crowding effects (15). In our system, however, we observe that the small SNAP protein is distributed throughout receptor-ligand enriched and depleted zones. These systems employ different proteins at the interface, and it will be interesting to investigate whether specific protein properties (e.g. size, propensity for oligomerization, elasticity, flexibility, packing density of receptor-ligand in partitioned zones, etc) account for these differences in the role of protein crowding in exclusion.

Our work also suggests an important contribution of receptor-ligand affinity in protein exclusion. We observed 70% depletion of CD45 R<sub>0</sub> from FRB-FKBP (100 fM K<sub>d</sub>) -enriched zones. The TCR-pMHC interactions, on the other hand, are much lower in affinity, with most agonists generally displaying K<sub>d</sub>s of 1-100  $\mu$ M (26). Strikingly, when we tested CD45 exclusion using TCR-pMHC, we found that exclusion was only 27% for the R<sub>0</sub> isoform and 49% for the R<sub>ABC</sub> isoform when tested individually. The PD-1-PD-L1 interaction is higher affinity (0.7 nM) and

produces a somewhat higher exclusion (60%) of CD45 R<sub>ABC</sub>. While the CD45 R<sub>0</sub> isoform exclusion by TCR-pMHC is modest, it nevertheless could be significant for eliciting a signaling response. *In vitro* analysis of the kinase-phosphatase network controlling TCR activation has shown that at physiological protein densities, small perturbations of CD45 can drive large changes in TCR phosphorylation (36). In combination with our results, this suggests that the cellular CD45 concentration may position the TCR precisely at the boundary of a switch-like response in phosphorylation.

Our experimental results also are in reasonable agreement with computational predictions for a lower boundary of receptor-ligand affinity needed for protein exclusion. Computational models by Weikl et al. (14) predict that, at the ratio of 1 TCR molecule to 8 CD45 molecules used in these experiments, a binding energy of  $>4 k_B T$  (corresponding to a K<sub>d</sub> of  $\sim 20 \mu M$ ) is required for partitioning. In our system, we find that a pMHC ligand with  $15 \mu M$  K<sub>d</sub> causes CD45 exclusion whereas a ligand with a K<sub>d</sub> of  $50 \mu M$  does not. It also has been predicted that increasing the affinity of a receptor-ligand interaction should increase the area fraction of the interface occupied by the receptor-ligand enriched zone by increasing the number of bound complexes at the same protein densities (14, 16). However, in our experiments, TCR-pMHC mediated CD45 partitioning occurs as an all-or-nothing process.

Our results also demonstrate that the large extracellular domains of CD45 R<sub>ABC</sub> and CD45 R<sub>0</sub> are differentially sensitive to the partitioning forces produced by ligand-receptor binding interactions at a membrane-membrane interface. This finding is consistent with results showing that T cells expressing larger CD45 isoforms signal more efficiently (37), although others have contested

this conclusion (38). Although the signaling consequences of differential CD45 segregation on immune activation remain to be clarified, our results establish a biophysical difference between two highly conserved CD45 isoforms (39) with regard to their degree of spatial segregation in response to TCR-pMHC interactions. Given that the smaller CD45 isoforms are preferentially expressed in later steps of T cell selection (22), our results suggest that T cell signaling may be attenuated by changes CD45 isoform expression as a mechanism of peripheral tolerance.

We also explore increasing complexity at a membrane interface by introducing two receptor-ligand pairs: TCR-pMHC and PD-1-PD-L1. Interestingly, we find that these two receptor-ligands complexes co-localize with one another and both together exclude CD45. *In vivo*, partial segregation of these two receptor-ligands also has been observed in CD8<sup>+</sup> T cells (40), and a higher degree of co-localization between these receptors was reported in CD4<sup>+</sup> T cells (30). Given that the size difference between the TCR-pMHC and PD-1-PD-L1 lies at the biophysical threshold for partitioning (15), these results suggest that cellular localization of PD-1 with respect to TCR may be regulated by other factors (e.g. other co-receptors or adaptor proteins) and perhaps even in cell type -specific manner. In addition, it will be interesting to investigate how actin polymer dynamics and lipid-mediated organization (41) may enhance or disrupt protein patterning across two membranes.

### **3.6 Materials and Methods**

**Materials.** Synthetic 1,2-dioleoyl-sn-glycero-3-phosphocholine (POPC; Avanti, 850457), 1,2-dioleoyl-sn-glycero-3-[(N-(5-amino-1-carboxypentyl)iminodiacetic acid)succinyl] (nickel salt, DGS-NTA-Ni; Avanti, 790404) and 1,2-dioleoyl-sn-glycero-3-phosphoethanolamine-N

[methoxy(polyethylene glycol)-5000] (ammonium salt, PEG5000-PE; Avanti, 880220) were acquired from Avanti Polar Lipids, Alabama, USA. 1,2-dioleoyl-sn-glycero-3-phosphoethanolamine-Atto390 (DOPE-390; AttoTec, AD390-161) was acquired from Atto-Tec, Germany.

**Recombinant protein expression, purification, and labeling.** N-terminally His<sub>10</sub>- and SNAP-tagged FRB and FKBP were subcloned into a pET28a vector and were bacterially expressed in BL21(DE3) strain of *Escherichia coli*. The cells were lysed in an Avestin Emulsiflex system. C-terminally His<sub>10</sub>- and SNAP- tagged extracellular domains of human CD45 R<sub>0</sub>, human CD45 R<sub>ABC</sub>, and human PD-L1 were subcloned into a pFastBac vector and were expressed in SF9 cells. All proteins were purified by using a HisTrap excel column (GE Healthcare Life Sciences) following the product recommendations. Recombinant C-terminal His<sub>10</sub>-tagged mouse PD-1 extracellular domain was purchased from Sino Biological.

2B4 TCR V<sub>m</sub>C<sub>h</sub> chimeras containing an engineered C domain disulfide were cloned into the pAcGP67a insect expression vector (BD Biosciences, 554756) encoding either a C-terminal acidic GCN4-zipper-Biotin acceptor peptide (BAP)-His<sub>6</sub> tag (for  $\alpha$  chain) or a C-terminal basic GCN4 zipper-His<sub>6</sub> tag (for  $\beta$  chain) (42). Thus the resulting dimer has a combined His<sub>12</sub>. Each chain also encoded a 3C protease site between the C-terminus of the TCR ectodomains and the GCN4 zippers to allow for cleavage of zippers. IE<sup>k</sup> MHC was cloned into pAcGP67A with acidic/basic zippers and His tags as described for TCRs. IE<sup>k</sup>  $\alpha$  and 2B4  $\alpha$  chain also encoded ybbr-tag sequence for direct protein labeling. The IE<sup>k</sup> $\beta$  construct was modified with an N-terminal extension containing either the 2A peptide via a Gly-Ser linker or CLIP peptide via a



Gly-Ser linker containing a thrombin cleavage site. Proteins were transiently expressed in High Five insect cells (BTI-TN-5B1-4) and purified using His-tag/Nickel according to published protocols (25).

For fluorescent labeling of SNAP-tagged proteins, 10  $\mu\text{M}$  protein was incubated with 20  $\mu\text{M}$  benzylguanine functionalized dye (New England Biolabs) in HBS buffer (50 mM HEPES, 150 mM NaCl, 1 mM TCEP, pH 7.4) for 1 h at room temperature or overnight on ice. For PD-L1 and TCR 10  $\mu\text{M}$  protein was incubated with 30  $\mu\text{M}$  tetramethylrhodamine-5-maleimide in HBS buffer for 1 h at room temperature. Excess dyes were removed using Zeba Spin Desalting Columns (ThermoFisher, 89882).

**Preparation of SNAP-DNA tethers.** Oligonucleotides were ordered from IDT with a 3'/5' terminal amine and labeled with BG-GLA-NHS as previously described (43). The adhesion strands used in this study consisted of a 3' 20mer region (5'- ACTGACTGACTGACTGACTG-3') with a 5' 80mer poly-dT and the complementary sequence (5'- CAGTCAGTCAGTCAGTCAGT-3') also with a 5' 80mer poly-dT. Conjugation to benzylguanine was performed as described (43). His<sub>10</sub>-tagged SNAP was labeled at a concentration of 5  $\mu\text{M}$  with a 3-fold excess of BG-DNA in HBS (50 mM HEPES, 150 mM NaCl and 1 mM TCEP, pH 7.4).

**Electroformation of giant unilamellar vesicles.** Lipids were mixed with a molar composition of 94.9% POPC, 5% DGS-NTA, 0.1% DOPE-390 in chloroform (Electron Microscopy Sciences, 12550) and dried under vacuum for 1 h to overnight. Electroformation was performed in 370

mM sucrose according to published protocols (44). GUVs were stored at room temperature and imaged within one week.

**Preparation of supported lipid bilayers.** Small unilamellar vesicles (SUVs) were prepared from a mixture of 97.5% POPC, 2% DGS-NGA-Ni, and 0.5% PEG5000-PE. The lipid mixture in chloroform was evaporated under argon and further dried under vacuum. The mixture was then rehydrated with phosphate buffered saline pH 7.4 and cycled between -80°C and 37°C 20 times, and then centrifuged for 45 min at 35,000 RCF. SUVs made by this method were stored at 4°C and used within two weeks of formation. Supported lipid bilayers were formed in freshly plasma cleaned custom PDMS chambers on RCA cleaned glass coverslips. 100  $\mu$ L of SUV solution containing 0.5 to 1 mg/ml lipid was added to the coverslips and incubated for 30 min. Unadsorbed vesicles were removed and bilayers were blocked by washing three times with reaction buffer (50 mM HEPES, 150 mM NaCl, 1 mM TCEP, 1 mg/mL bovine serum albumen, pH 7.4), and incubating for 20 min.

**Optical setup for spinning disk, total internal reflection fluorescence, and scanning angle interference microscopy.** Imaging was performed on one of two Nikon TI-E microscopes equipped with a Nikon 60x Plan Apo VC 1.20 NA water immersion objective, or a Nikon 100x Plan Apo 1.49 NA oil immersion objective, and four laser lines (405, 488, 561, 640 nm), either a Hamamatsu Flash 4.0 or Andor iXon EM-CCD camera, and  $\mu$ Manager software (45). A polarizing filter was placed in the excitation laser path to polarize the light perpendicular to the plane of incidence. Angle of illumination was controlled with either a standard Nikon TIRF motorized positioner or a mirror moved by a motorized actuator (Newport, CMA-25CCCL).

Scanning angle microscopy was performed and analyzed as previously described (23). For FRAP experiments, a region of  $\sim 1 \mu\text{m}^2$  was photobleached using a 405 nm laser modulated by a Rapp UGA-40 photo targeting unit and the fluorescence recovery was monitored over time.

**Reconstitution of membrane interfaces.** GUVs and SLBs were separately incubated for one hour with the indicated proteins for each experiment. Proteins were diluted in reaction buffer (50 mM HEPES, 150 mM NaCl, 1 mM TCEP, 1 mg/mL bovine serum albumen, pH 7.4) and then mixed 2:1 with GUVs, or added to supported lipid bilayers. SLBs were washed 6 times with  $\frac{1}{2}$  total well volume resulting in a final concentration of  $\sim 1\%$  input protein remaining. The GUVs were not washed but were diluted 10-fold into the imaging well with the supported lipid bilayer after a one hour incubation. Rapamycin (Sigma, R0395) was added to FRB-FKBP reactions at a final concentration of  $5 \mu\text{M}$ . GUVs were allowed to settle for 30-60 min prior to imaging. SLB fluidity was assessed by visualizing diffusion of unbound GUV proteins that associate with the supported lipid bilayer (e.g. FKBP, TCR, CD45). If  $>25\%$  of fluorescent molecules on the SLB were not diffusive, the experiment was repeated with a more fluid bilayer.

**Estimated protein densities.** Protein densities are estimates based on the conversion factor between protein concentration and molecular density defined by Schmid, et al (15). Given our system utilizes an analogous physical setup to their experiments, including the same homemade PDMS-wells with 100uL volume (described in “Preparation of supported lipid bilayers” section of the Methods) and protein concentrations in a similar range (1-100nM), we can extrapolate from their measurement of  $2,317 \pm 370$  molecules/ $\mu\text{m}^2$  for an SLB with 2.5% DGS-NTA-Ni incubated with 100 nM His<sub>10</sub>-tagged protein. Because the SLBs used in this study contain 2%

DGS-NTA-Ni and GUVs contain 5% DGS-NTA-Ni, this factor (23.17 molec/ $\mu\text{m}^2/\text{nM}$ ) was first multiplied by 0.8 or 2, respectively. Protein concentrations (in nM) were then multiplied by the membrane-specific scaling factor to give an estimated final density in molecules/ $\mu\text{m}^2$ . This estimate may be imperfect due to differences in specific experimental variables affecting total lipid surface area available for protein binding including differences in electroformation. These estimated densities are: FKBP (5-200 molec/ $\mu\text{m}^2$ ), CD45 R0 and RABC (1000 molec/ $\mu\text{m}^2$ ), TCR (200 molec/ $\mu\text{m}^2$ ), PD-L1 (50 molec/ $\mu\text{m}^2$ ), SNAP (50 molec/ $\mu\text{m}^2$ ), PD-1 (100-300 molec/ $\mu\text{m}^2$ ), MHC (200 molec/ $\mu\text{m}^2$ ), FRB (20 molec/ $\mu\text{m}^2$ ).












**Image analysis.** Images were analyzed using ImageJ (FIJI) (46). The same brightness and contrast were applied to images within the same panels. FIJI rolling ball background subtraction was applied to images before calculating mean fluorescence intensities. Percent exclusion was calculated as one minus the ratio of average intensity inside a receptor enriched zone to the average intensity at the interface outside the receptor-enriched zone. ROIs for inside and outside receptor-enriched zones were selected manually within regions of comparable lipid intensity. All exclusion quantification refers to images acquired using TIRF microscopy. Data from image analysis within FIJI was graphed using Microsoft Excel.

**Liposome Assay.** Experiments were carried out as previously described (28). Briefly, proteins were purified using baculovirus or bacterial expression system. LUVs and proteins of interest were premixed and incubated at room temperature for 1 h. 2 mM ATP was then injected and rapidly mixed to trigger Lck mediated phosphorylation of CD3 $\zeta$  and PD-1. 20 minutes after ATP addition, apyrase was added ( $t = 0$  min) and the reactions were allowed to continue at room

temperature. Equal fractions of the reactions were removed and terminated with SDS sample buffer at the indicated time points. Anti-phosphotyrosine antibody (pY20, Santa Cruz Biotechnology #SC-508) was used to detect phosphorylation by western blotting.

### 3.7 Supporting Information

**Table S1. Protein extracellular domain size estimates**

	Protein	Size estimate	Notes	References
	FKBP	4 nm	Distance from FKBP Arg 13 to Thr 85 from PDB 3FAP measured in Chimera software.	Liang et al. 1999
	FRB	4 nm	Distance from FRB Gln 152 to Asn 182 from PDB 3FAP measured in Chimera software.	Liang et al. 1999
	FKBP-FRB complex	6 nm	Distance from FKBP Thr 6 to FRB Gln 152 from PDB 3FAP measured in Chimera software.	Liang et al. 1999
	CD45 R <sub>0</sub>	25 nm	Estimate based on published electron microscopy and crystallographic studies.	Woollett et al. 1985, McCall et al. 1992, Chang et al. 2016
	CD45 R <sub>ABC</sub>	40 nm	Estimate based on published electron microscopy and crystallographic studies.	Woollett et al. 1985, McCall et al. 1992, Chang et al. 2016
	TCR	7 nm	Distance from TCR β Asp 244 to TCR α Thr 92 from PDB 4P2O measured in Chimera software.	Birnbaum et al. 2014
	pMHC	7 nm	Distance from MHC β Pro 165 to Pro 65 from PDB 4P2O measured in Chimera software.	Birnbaum et al. 2014
	TCR-pMHC complex	13 nm	Distance from TCR β Asp 244 to MHC β Pro 165 from PDB 4P2O measured in Chimera software.	Birnbaum et al. 2014
	PD-1	5 nm	Distance from Pro 130 to Ile 148 from PDB 3BIK measured in Chimera software.	Lin et al. 2008
	PD-L1	8 nm	Distance from Gln 47 to Leu 229 from PDB 3BIK measured in Chimera software.	Lin et al. 2008
	PD-1-PD-L1 complex	9 nm	Distance from PD-L1 Leu 229 to PD-1 Ile 148 from PDB 3BIK measured in Chimera software.	Lin et al. 2008
-	SNAP	5 nm	Distance from Ala 50 to Leu 153 from PDB 3KZY measured in Chimera software.	Schmitt et al. 2010
-	DNA tether	125 nm	Assuming 0.34 nm per double stranded base pair (20 bp) and 0.67 nm per single stranded base pair (160 bp) plus 5 nm for each of two SNAP proteins. At this length the DNA tether is expected to be quite flexible.	Chi et al, 2013

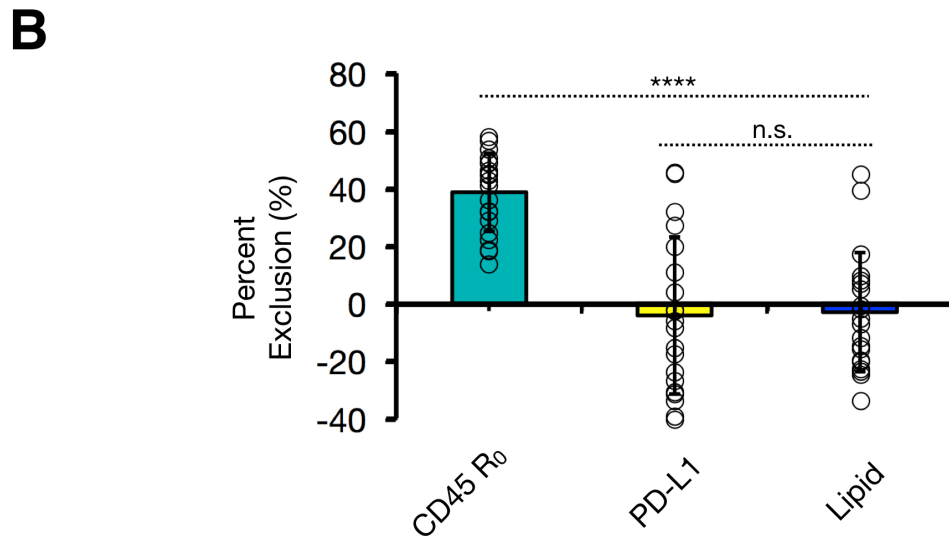
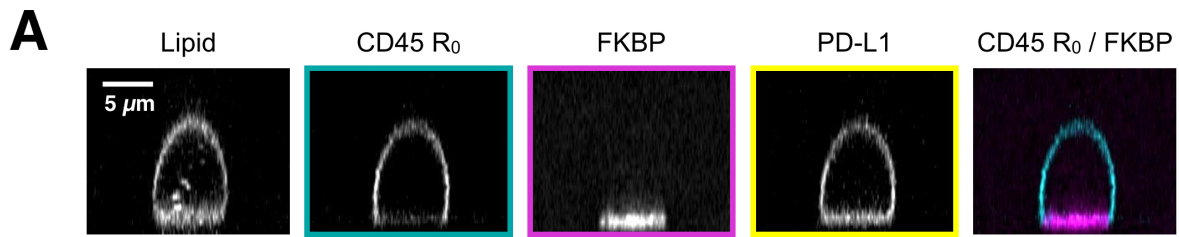


**Fig. S1.** PD-L1 is not excluded from FKBP-bound membrane interfaces. **(A)** Spinning disk z-sections of GUVs after membrane-apposed interfaces have reached equilibrium, showing localization of FKBP to the membrane interface, localization of CD45 R<sub>0</sub> away from the interface, and uniform distribution of PD-L1. **(B)** Quantification of experiment shown in A; mean ± standard deviation (n=20 GUVs pooled from two experiments).

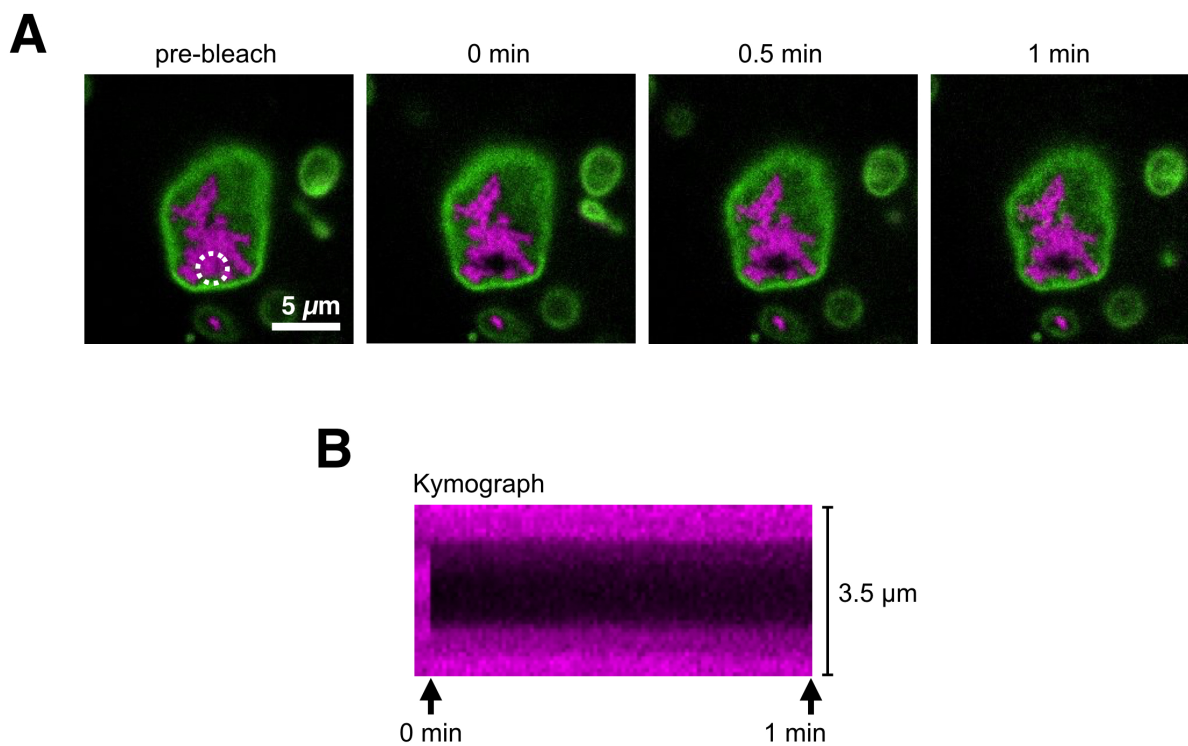


**Fig. S2.** FKBP molecules in partitioned domains do not readily exchange. **(A)** Images for FKBP enriched interfaces before and after photobleaching (dashed white line, bleach site). Scale bars, 5  $\mu\text{m}$  **(B)** Kymograph corresponding to **A**. Data are representative of three independent experiments.

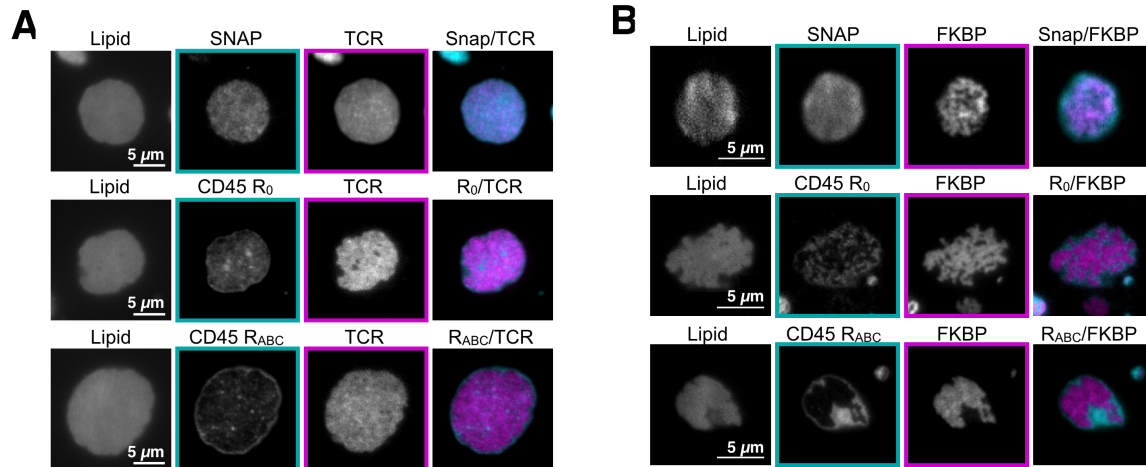


**Fig. S3.** TCR-pMHC and FRB-FKBP exclude CD45 R<sub>0</sub> and CD45 R<sub>ABC</sub> but not SNAP. **(A)** TIRF microscopy of a GUV-SLB interface at equilibrium showing concentration of TCR into microdomains. Top, SNAP is homogeneously distributed. Middle, CD45 R<sub>0</sub> is weakly excluded. Bottom, CD45 R<sub>ABC</sub> is strongly excluded. **(B)** TIRF microscopy of a GUV-SLB interface at equilibrium showing concentration of FKBP into micro domains. SNAP is homogeneously distributed. CD45 R<sub>0</sub> and CD45 R<sub>ABC</sub> are excluded.



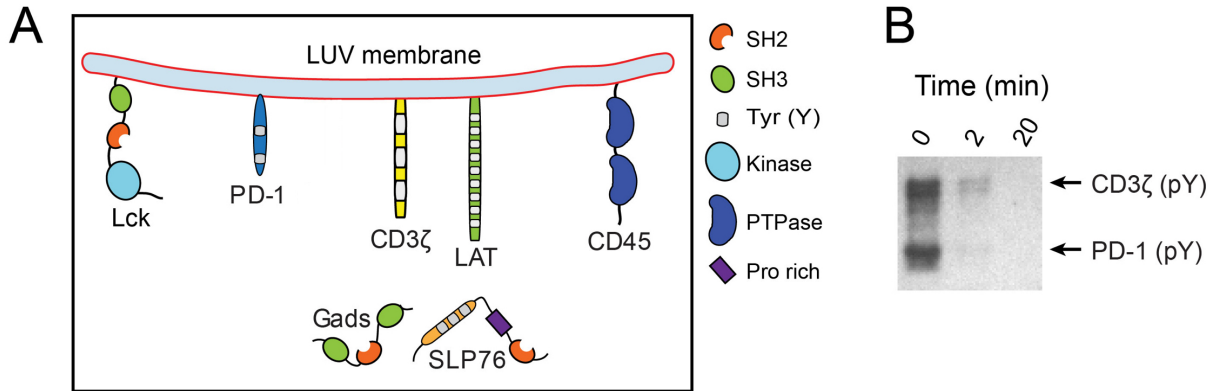


**Fig. S4.** PD-1 is a target for CD45 dephosphorylation. (A) Schematic of LUV reconstitution system for assaying the sensitivity PD-1 to CD45. DGS-NTA-Ni containing LUVs were attached with purified, polyhistidine-tagged cytosolic domains of receptors (CD3 $\zeta$  [290 molecules per  $\mu\text{m}^2$ ]; PD-1 [870 molecules per  $\mu\text{m}^2$ ]), the adaptor LAT (870 molecules per  $\mu\text{m}^2$ ), the kinase Lck (290 molecules per  $\mu\text{m}^2$ ), and the phosphatase CD45 (29 molecules per  $\mu\text{m}^2$ ). Purified cytosolic factors (Gads [0.3  $\mu\text{M}$ ]; SLP76 [0.3  $\mu\text{M}$ ]) were added to solution to create a more physiological setting. Pre-addition of ATP triggered net phosphorylation of both CD3 $\zeta$  and PD-1 by Lck, despite the presence of CD45, owing to the 10-fold excess of Lck over CD45. (B) A phosphotyrosine western blot showing the time course of CD3 $\zeta$  and PD-1 dephosphorylation by CD45, after the addition of the ATP scavenger Apyrase, which rapidly terminated the Lck kinase activity to isolate the CD45 activity. PTPase, protein tyrosine phosphatase; Pro, proline.

### 3.8 Author Contributions

Author contributions: C.B.C., N.K., E.H., X.S., and R.D.V. designed research; C.B.C., N.K., and E.H. performed research; C.B.C., N.K., R.A.F., E.H., X.S., and K.C.G. contributed new reagents/analytic tools; C.B.C. and N.K. analyzed data; and C.B.C., N.K., and R.D.V. wrote the paper.

### 3.9 Acknowledgements

We would like to thank N. Stuurman for help with microscopy and image analysis and M. Taylor for guidance with protein purification and DNA tethering. We thank A. Williamson, N. Stuurman, and M. Morrissey for comments on the manuscript. The authors acknowledge funding from the Howard Hughes Medical Institute and National Institutes of Health (R01EB007187, R.D.V.).

### 3.10 References

1. Brownlie RJ, Zamoyska R (2013) T cell receptor signalling networks: branched, diversified and bounded. *Nat Rev Immunol* 13(4):257–269.
2. Davis SJ, van der Merwe PA (2006) The kinetic-segregation model: TCR triggering and beyond. *Nat Immunol* 7(8):803–809.
3. Woollett GR, Williams AF, Shotton DM (1985) Visualisation by low-angle shadowing of the leucocyte-common antigen. A major cell surface glycoprotein of lymphocytes. *EMBO J* 4(11):2827–30.

4. McCall MN, Shotton DM, Barclay AN (1992) Expression of soluble isoforms of rat CD45. Analysis by electron microscopy and use in epitope mapping of anti-CD45R monoclonal antibodies. *Immunology* 76(2):310–7.
5. Chang VT, et al. (2016) Initiation of T cell signaling by CD45 segregation at “close contacts.” *Nat Immunol* 17(5):574–582.
6. Garcia KC, et al. (1996) An  $\alpha\beta$  T Cell Receptor Structure at 2.5 Å and Its Orientation in the TCR-MHC Complex. *Science* (80-) 274(5285):209–219.
7. Choudhuri K, Wiseman D, Brown MH, Gould K, van der Merwe PA (2005) T-cell receptor triggering is critically dependent on the dimensions of its peptide-MHC ligand. *Nature* 436(7050):578–582.
8. Leupin O, Zaru R, Laroche T, Müller S, Valitutti S (2000) Exclusion of CD45 from the T-cell receptor signaling area in antigen-stimulated T lymphocytes. *Curr Biol* 10(5):277–280.
9. Johnson KG, Bromley SK, Dustin ML, Thomas ML (2000) A supramolecular basis for CD45 tyrosine phosphatase regulation in sustained T cell activation. *Proc Natl Acad Sci* 97(18):10138–10143.
10. Varma R, Campi G, Yokosuka T, Saito T, Dustin ML (2006) T Cell Receptor-Proximal Signals Are Sustained in Peripheral Microclusters and Terminated in the Central Supramolecular Activation Cluster. *Immunity* 25(1):117–127.
11. James JR, Vale RD (2012) Biophysical mechanism of T-cell receptor triggering in a reconstituted system. *Nature* 487:64–69.
12. Cordoba S-P, et al. (2013) The large ectodomains of CD45 and CD148 regulate their segregation from and inhibition of ligated T-cell receptor. *Blood* 121(21):4295–4302.

13. Lee S-JE, Hori Y, Chakraborty AK (2003) Low T cell receptor expression and thermal fluctuations contribute to formation of dynamic multifocal synapses in thymocytes. *Proc Natl Acad Sci* 100(8):4383–4388.
14. Weikl TR, Lipowsky R (2004) Pattern Formation during T-Cell Adhesion. *Biophys J* 87(6):3665–3678.
15. Schmid EM, et al. (2016) Size-dependent protein segregation at membrane interfaces. *Nat Phys* 12(7):704–711.
16. Chung M, Koo BJ, Boxer SG (2013) Formation and analysis of topographical domains between lipid membranes tethered by DNA hybrids of different lengths. *Faraday Discuss* 161:333–345.
17. Banaszynski LA, Liu CW, Wandless TJ (2005) Characterization of the FKBP·Rapamycin·FRB Ternary Complex. *J Am Chem Soc* 127(13):4715–4721.
18. Taylor MJ, Husain K, Gartner ZJ, Mayor S, Vale RD (2016) *Signal Transduction Through a DNA-Based T Cell Receptor* doi:10.1101/062877.
19. Chi Q, Wang G, Jiang J (2013) The persistence length and length per base of single-stranded DNA obtained from fluorescence correlation spectroscopy measurements using mean field theory. *Phys A Stat Mech its Appl* 392(5):1072–1079.
20. Gautier A, et al. (2008) An Engineered Protein Tag for Multiprotein Labeling in Living Cells. *Chem Biol* 15(2):128–136.
21. Bannwarth M, et al. Crystal structure of SNAP-tag. *doi.org*. doi:10.2210/pdb3kzy/pdb.
22. Hermiston ML, Xu Z, Weiss A (2003) CD45: A Critical Regulator of Signaling Thresholds in Immune Cells. *Annu Rev Immunol* 21(1):107–137.
23. Carbone CB, Vale RD, Stuurman N (2016) *A data acquisition and analysis pipeline for*

- scanning angle interference microscopy* doi:10.1101/050468.
24. Liang J, Choi J, Clardy J (1999) Refined structure of the FKBP12-rapamycin-FRB ternary complex at 2.2 Å resolution. *Acta Crystallogr D Biol Crystallogr* 55(Pt 4):736–44.
  25. Birnbaum ME, et al. (2014) Deconstructing the Peptide-MHC Specificity of T Cell Recognition. *Cell* 157(5):1073–1087.
  26. Gascoigne NRJ, Zal T, Alam SM (2001) T-cell receptor binding kinetics in T-cell development and activation. *Expert Rev Mol Med* 3(6). doi:10.1017/S1462399401002502.
  27. Chen L, Flies DB (2013) Molecular mechanisms of T cell co-stimulation and co-inhibition. *Nat Rev Immunol* 13(4):227–242.
  28. Hui E, et al. (2016) *T cell co-stimulatory receptor CD28 is a primary target for PD-1-mediated inhibition* doi:10.1101/086652.
  29. Kamphorst AO, et al. (2017) Rescue of exhausted CD8 T cells by PD-1–targeted therapies is CD28-dependent. *Science (80- )* 355(6332):1423–1427.
  30. Yokosuka T, et al. (2012) Programmed cell death 1 forms negative costimulatory microclusters that directly inhibit T cell receptor signaling by recruiting phosphatase SHP2. *J Exp Med* 209(6):1201–1217.
  31. Sheppard K-A, et al. (2004) PD-1 inhibits T-cell receptor induced phosphorylation of the ZAP70/CD3 $\zeta$  signalosome and downstream signaling to PKC $\theta$ . *FEBS Lett* 574(1–3):37–41.
  32. Lin DY -w., et al. (2008) The PD-1/PD-L1 complex resembles the antigen-binding Fv domains of antibodies and T cell receptors. *Proc Natl Acad Sci* 105(8):3011–3016.
  33. Butte MJ, Peña-Cruz V, Kim M-J, Freeman GJ, Sharpe AH (2008) Interaction of human PD-L1 and B7-1. *Mol Immunol* 45(13):3567–3572.

34. Burroughs NJ, Wülfing C (2002) Differential Segregation in a Cell-Cell Contact Interface: The Dynamics of the Immunological Synapse. *Biophys J* 83(4):1784–1796.
35. Krobath H, Różycki B, Lipowsky R, Weikl TR (2011) Line Tension and Stability of Domains in Cell-Adhesion Zones Mediated by Long and Short Receptor-Ligand Complexes. *PLoS One* 6(8):e23284.
36. Hui E, Vale RD (2014) In vitro membrane reconstitution of the T-cell receptor proximal signaling network. *Nat Struct Mol Biol* 21(2):133–42.
37. Chui D, Ong CJ, Johnson P, Teh HS, Marth JD (1994) Specific CD45 isoforms differentially regulate T cell receptor signaling. *EMBO J* 13(4):798–807.
38. Czyzyk J, Leitenberg D, Taylor T, Bottomly K (2000) Combinatorial Effect of T-Cell Receptor Ligation and CD45 Isoform Expression on the Signaling Contribution of the Small GTPases Ras and Rap1. *Mol Cell Biol* 20(23):8740–8747.
39. Okumura M, et al. (1996) Comparison of CD45 extracellular domain sequences from divergent vertebrate species suggests the conservation of three fibronectin type III domains. *J Immunol* 157(4):1569–75.
40. Hui E, et al. (2017) T cell costimulatory receptor CD28 is a primary target for PD-1–mediated inhibition. *Science (80- )* 355(6332):1428–1433.
41. Köster D V, Mayor S (2016) Cortical actin and the plasma membrane: inextricably intertwined. *Curr Opin Cell Biol* 38:81–89.
42. Wilson DB, et al. (1999) Immunogenicity. I. Use of peptide libraries to identify epitopes that activate clonotypic CD4+ T cells and induce T cell responses to native peptide ligands. *J Immunol* 163(12):6424–34.
43. Farlow J, et al. (2013) Formation of targeted monovalent quantum dots by steric

- exclusion. *Nat Methods* 10(12):1203–1205.
44. Schmid EM, Richmond DL, Fletcher DA (2015) Reconstitution of proteins on electroformed giant unilamellar vesicles, pp 319–338.
  45. Edelstein A, Amodaj N, Hoover K, Vale R, Stuurman N (2010) Computer Control of Microscopes Using  $\mu$ Manager. *Current Protocols in Molecular Biology* (John Wiley & Sons, Inc., Hoboken, NJ, USA). doi:10.1002/0471142727.mb1420s92.
  46. Schindelin J, et al. (2012) Fiji: an open-source platform for biological-image analysis. *Nat Methods* 9(7):676–82.

## CHAPTER 4

### **Concluding thoughts**



## 4.1 Conclusion

Although the evidence that CD45 partitions away from bound TCR-pMHC pairs is extremely strong, understanding how protein partitioning might cooperate with other possible mechanisms of T cell triggering remains an open question. A major caveat for kinetic segregation is that it is not yet definitively clear how the specificity and sensitivity of a T cell could be achieved through a CD45 partitioning mechanism. The work presented in this thesis suggests that affinity and CD45 isoform expression influence partitioning, but other binding parameters have been proposed to predict the potency of TCR signaling, as well. Additionally, other factors have been suggested to regulate CD45 partitioning, including lipid organization or microcluster formation.

**Lipid organization.** Lipid rafts have been hypothesized to influence TCR signaling by contributing to membrane organization. Early evidence showed that TCR appears in a detergent insoluble “raft” fraction when bound to stimulating antibody. Because CD45 was determined to be a “non-raft” protein by this assay, induced translocation of the TCR into rafts was proposed as an additional mechanism to protect the TCR from dephosphorylation by CD45 by spatial segregation.<sup>1</sup> In contrast, work from Adam Douglass in the Vale lab found that protein-protein interactions, and not lipid raft associations, are the stronger driving force in synapse formation, and the diffusional behaviors of different proteins in the T cell signaling pathway vary significantly but do not correlate with biochemical fractionation into lipid rafts.<sup>2</sup> This discrepancy could be explained by the fact that detergents can induce aggregations in lipid mixtures, making rafts an artificial byproduct of the extraction method.<sup>3</sup> However, recent super resolution microscopy data has suggested that lipid mediated forces still may operate on very short length scales to bias signaling networks.<sup>4</sup> Though lipid organization is not necessary for

partitioning based on extracellular domain size, understanding to what extent it may (or may not) tune signaling thresholds will be important for a comprehensive understanding of T cell triggering.

**Microcluster formation.** During T cell activation, signaling proteins organize phase separated clusters based on weak multivalent interactions and electrostatic charge. In a simplified reconstitution system, the negative charge on the CD45 cytoplasmic domain was sufficient to partition CD45 away from LAT clusters.<sup>6</sup> This phosphatase exclusion mechanism would also favor phosphorylation within the clusters, similar to an exclusion mechanism based on extracellular domain size. However, at the initial stages of T cell receptor triggering, LAT clusters would not have formed. Therefore, charge-based exclusion of CD45 likely reinforces partitioning at later stages of T cell activation, rather than accounting for the initial receptor triggering.

**Binding properties.** The biophysical TCR-pMHC interaction parameters that have been proposed to predict signaling potency include affinity, kinetics, 2D confinement time, and 2D on-rate;<sup>7-9</sup> and structural parameters include conformational change, docking geometry, and complex stability.<sup>10-17</sup> Recent work from Chris Garcia's lab by Leah Sibener suggests a model in which catch bond formation might be the important parameter unifying TCR intrinsic determinants of signal potency with extrinsic determinants like CD45 segregation (in press). In this model, interaction of a TCR and pMHC is sustained by the formation of a catch bond, which allows for local CD45 segregation, and thus TCR triggering and subsequent downstream activation. Catch bond formation may increase either the probability of CD45 exclusion or the

dwelling time of bound TCR/pMHC in areas from which CD45 is segregated. When tested in a GUV partitioning assay, not all receptor-ligand binding events have the ability to promote CD45 exclusion, and signaling-deficient TCR-pMHC interactions do not show CD45 segregation.

Developing a unified, predictive model of the relationship between TCR-pMHC biophysical interactions and T cell signaling will require additional study. As our understanding of TCR triggering progresses, we may uncover paradigms that are generalizable to other signaling systems.

## 4.2 References

1. Janes PW, Ley SC, Magee AI (1999) Aggregation of lipid rafts accompanies signaling via the T cell antigen receptor. *J Cell Biol* 147(2):447–61.
2. Douglass AD, Vale RD (2005) Single-molecule microscopy reveals plasma membrane microdomains created by protein-protein networks that exclude or trap signaling molecules in T cells. *Cell* 121(6):937–50.
3. Heerklotz H (2002) Triton promotes domain formation in lipid raft mixtures. *Biophys J* 83(5):2693–701.
4. Stone MB, Shelby SA, Núñez MF, Wisser K, Veatch SL (2017) Protein sorting by lipid phase-like domains supports emergent signaling function in B lymphocyte plasma membranes. *Elife* 6. doi:10.7554/eLife.19891.
5. Su X, et al. (2016) Phase separation of signaling molecules promotes T cell receptor signal transduction. *Science* (80- ) 352(6285):595–599.
6. Aleksic M, et al. (2010) Dependence of T cell antigen recognition on T cell receptor-peptide MHC confinement time. *Immunity* 32(2):163–74.

7. Bidot C, et al. Mathematical modeling of T-cell activation kinetic. *J Comput Biol* 15(1):105–28.
8. Huppa JB, et al. (2010) TCR-peptide-MHC interactions in situ show accelerated kinetics and increased affinity. *Nature* 463(7283):963–7.
9. Baumgartner CK, Malherbe LP (2010) Regulation of CD4 T-cell receptor diversity by vaccine adjuvants. *Immunology* 130(1):16–22.
10. Beddoe T, et al. (2009) Antigen ligation triggers a conformational change within the constant domain of the alphabeta T cell receptor. *Immunity* 30(6):777–88.
11. Cochran JR, Cameron TO, Stone JD, Lubetsky JB, Stern LJ (2001) Receptor Proximity, Not Intermolecular Orientation, Is Critical for Triggering T-cell Activation. *J Biol Chem* 276(30):28068–28074.
12. Gras S, et al. (2016) Reversed T Cell Receptor Docking on a Major Histocompatibility Class I Complex Limits Involvement in the Immune Response. *Immunity* 45(4):749–760.
13. He Y, et al. (2015) Identification of the Docking Site for CD3 on the T Cell Receptor  $\beta$  Chain by Solution NMR. *J Biol Chem* 290(32):19796–19805.
14. Kim ST, et al. (2009) The alphabeta T cell receptor is an anisotropic mechanosensor. *J Biol Chem* 284(45):31028–37.
15. Krogsgaard M, et al. (2003) Evidence that structural rearrangements and/or flexibility during TCR binding can contribute to T cell activation. *Mol Cell* 12(6):1367–78.
16. Natarajan K, et al. (2017) An allosteric site in the T-cell receptor C $\beta$  domain plays a critical signalling role. *Nat Commun* 8:15260.
17. Pullen RH, Abel SM (2017) Catch Bonds at T Cell Interfaces: Impact of Surface Reorganization and Membrane Fluctuations. *Biophys J* 113(1):120–13

## **Publishing Agreement**

It is the policy of the University to encourage the distribution of all theses, dissertations, and manuscripts. Copies of all UCSF theses, dissertations, and manuscripts will be routed to the library via the Graduate Division. The library will make all theses, dissertations, and manuscripts accessible to the public and will preserve these to the best of their abilities, in perpetuity.

I hereby grant permission to the Graduate Division of the University of California, San Francisco to release copies of my thesis, dissertation, or manuscript to the Campus Library to provide access and preservation, in whole or in part, in perpetuity.

Author Signature:  \_\_\_\_\_ Date: June 15, 2018